

STOCHASTIC MODELING OF MULTIWAVELENGTH VARIABILITY OF THE CLASSICAL BL LAC OBJECT OJ 287 ON TIMESCALES RANGING FROM DECADES TO HOURS

A. GOYAL¹, L. STAWARZ¹, S. ZOLA^{1,2}, V. MARCHENKO¹, M. SOIDA¹, K. NILSSON³, S. CIPRINI^{4,5}, A. BARAN², M. OSTROWSKI¹, P. J. WITA⁶, GOPAL-KRISHNA⁷, A. SIEMIGINOWSKA⁸, M. SOBOLEWSKA⁸, S. JORSTAD^{9,10}, A. MARSCHER¹⁰, M. F. ALLER¹¹, H. D. ALLER¹¹, T. HOVATTA³, D. B. CATON¹², D. REICHART¹³, K. MATSUMOTO¹⁴, K. SADAKANE¹⁴, K. GAZEAS¹⁵, M. KIDGER¹⁶, V. PIROLA^{17,3}, H. JERMAK¹⁸, F. ALICAVUS^{19,20}, K. S. BALIYAN²¹, A. BARANSKY²², A. BERDYUGIN⁶, P. BLAY²³, P. BOUMIS²⁴, D. BOYD²⁵, Y. BUFAN^{26,27}, M. CAMPAS TORRENT²⁸, F. CAMPOS²⁹, J. CARRILLO GÓMEZ³⁰, J. DALESSIO³¹, B. DEBSKI¹, D. DIMITROV³², M. DROZDZ², H. ER³³, A. ERDEM^{19,20}, A. ESCARTIN PÉREZ³⁴, V. FALLAH RAMAZANI³, A. V. FILIPPENKO³⁵, E. GAFTON³⁶, F. GARCIA³⁷, V. GODUNOVA²⁶, F. GÓMEZ PINILLA³⁸, M. GOPINATHAN³⁹, J. B. HAISLIP⁴⁰, S. HAQUE⁴¹, J. HARMANEN³, R. HUDEC^{43,44}, G. HURST⁴⁵, K. M. IVARSEN⁴⁰, A. JOSHI³⁹, M. KAGITANI⁴⁶, N. KARAMAN⁴⁷, R. KARJALAINEN⁴⁸, N. KAUR²¹, D. KOZIEL-WIERZBOWSKA¹, E. KULIGOWSKA¹, T. KUNDERA¹, S. KUROWSKI¹, A. KVAMMEN³⁶, A. P. LACLUYZE⁴⁰, B. C. LEE⁴⁹, A. LIAKOS²⁴, J. LOZANO DE HARO⁵⁰, I. MOHAMMED⁴¹, J. P. MOORE⁴⁰, M. MUGRAUER⁵¹, R. NAVES NOGUES²⁸, A. W. NEELY⁵², W. OGLOZA², S. OKANO⁴⁷, U. PAJDOSZ¹, J. C. PANDEY³⁹, M. PERRI^{4,53}, G. POYNER⁵⁵, J. PROVENCAL³¹, T. PURSIMO³⁶, A. RAJ⁵⁵, B. RAJKUMAR⁴¹, R. REINTHAL³, T. REYNOLDS³⁶, J. SAARIO³⁶, S. SADEGI⁵⁶, T. SAKANOI⁴⁶, J. L. SALTO GONZÁLEZ⁵⁷, SAMEER⁵⁸, A. O. SIMON⁵⁹, M. SIWAK², T. SCHWEYER^{60,61}, F. C. SOLDÁN ALFARO⁶², E. SONBAS⁴⁷, J. STROBL⁴², L. O. TAKALO³, L. TREMOSA ESPASA⁶³, J. R. VALDES⁶⁴, V. V. VASYLENKO⁵⁹, F. VERRECCHIA^{4,53}, J. R. WEBB⁶⁵, M. YONEDA⁶⁶, M. ZEJMO⁶⁷, W. ZHENG³⁵, P. ZIELINSKI⁶⁸, J. JANIK⁶⁸, V. CHAVUSHYAN⁶⁴,

Draft version September 15, 2017

ABSTRACT

We present the results of our power spectral analysis for the BL Lac object OJ 287, utilizing the *Fermi*-LAT survey at high-energy γ -rays, the *Swift*-XRT data in X-rays, several ground-based telescopes and the *Kepler* satellite in optical, and single-dish GHz-band radio telescopes. The multiwavelength light curves of the source are modeled in terms of a continuous-time auto regressive moving average (CARMA) process. Due to the inclusion of the *Kepler* data, we were able to construct *for the first time* the optical variability power spectrum without any gaps across ~ 6 dex in temporal frequencies. Our analysis reveals that the power spectra derived at radio frequencies are of a pure red-noise type on the timescales ranging from tens of years down to months. The overall optical power spectrum is also consistent with a red noise on the variability timescales ranging from 117 years down to hours, with no hints for any quasi-periodic oscillations, but instead a break near variability timescales ~ 1 day. The power spectrum derived at X-ray photon energies resembles the radio and optical power spectra on the analogous timescales. Finally, the high-energy γ -ray power spectrum of OJ 287 is noticeably different from the radio, optical, and X-ray power spectra of the source: we have detected the characteristic relaxation timescale in the *Fermi*-LAT data, corresponding to $\simeq 100$ days, such that on the timescales longer than this, the power spectrum is consistent with an uncorrelated (white) noise, while on the shorter variability timescales with a correlated (colored) noise.

Keywords: acceleration of particles — magnetic fields — radiation mechanisms: non-thermal — galaxies: active — BL Lacertae objects: individual (OJ 287) — galaxies: jets

email: arti@oa.uj.edu.pl

¹ Astronomical Observatory of Jagiellonian University, ul. Orla 171, 30-244 Kraków, Poland

² Mt. Suhora Observatory, Pedagogical University, ul. Podchorążych 2, Kraków 30-084, Poland

³ Tuorla Observatory, Department of Physics and Astronomy, University of Turku, Turku F-21500, Finland

⁴ Agenzia Spaziale Italiana (ASI) Science Data Center, Roma I-00133, Italy

⁵ Istituto Nazionale di Fisica Nucleare, Sezione di Perugia, Perugia I-06123, Italy

⁶ Department of Physics, The College of New Jersey, 2000 Pennington Rd., Ewing, NJ 08628-0718, USA

⁷ Centre for Excellence in Basic Sciences (CEBS), University of Mumbai campus (Kalina), Mumbai 400098, India

⁸ Harvard Smithsonian Center for Astrophysics, 60 Garden St, Cambridge, MA 02138, USA

⁹ Institute for Astrophysical Research, Boston University, 725 Commonwealth Avenue, Boston, MA 02215, USA

¹⁰ Astronomical Institute, St. Petersburg State University, Universitetskij Pr. 28, Petrodvorets, 198504 St. Petersburg, Russia

¹¹ Astronomy Department, University of Michigan, Ann

Arbor, MI, USA

¹² Dark Sky Observatory, Department of Physics and Astronomy, Appalachian State University, Boone, NC 28608, USA

¹³ Department of Physics and Astronomy, University of North Carolina, Chapel Hill, NC 27599, USA

¹⁴ Astronomical Institute, Osaka Kyoiku University, 4-698 Asahigaoka, Kashiwara, Osaka 582-8582, Japan

¹⁵ Section of Astrophysics, Astronomy and Mechanics, Department of Physics, National & Kapodistrian University of Athens, Zografos GR-15784, Athens, Greece

¹⁶ Herschel Science Centre, ESAC, European Space Agency, C/Bajo el Castillo, s/n, Villanueva de la Cañada E-28692, Madrid, Spain

¹⁷ Finnish Centre for Astronomy with ESO, University of Turku, TurkuF-21500, Finland

¹⁸ Astrophysics Research Institute, Liverpool John Moores University, IC2, Liverpool Science Park, Brownlow Hill L3 5RF, UK

¹⁹ Department of Physics, Faculty of Arts and Sciences, Canakkale Onsekiz Mart University, Canakkale TR-17100, Turkey

²⁰ Astrophysics Research Center and Ulupinar Observatory, Canakkale Onsekiz Mart University, Canakkale TR-17100,

1. INTRODUCTION

Blazars are a major class of active galactic nuclei (AGN), whose total radiative energy output is dominated by the Doppler-boosted, broad-band, and non-thermal emission of relativistic jets launched by accreting super-massive black holes from the centers of massive elliptical galaxies (Begelman et al. 1984; de Young 2002; Meier

2012). The blazar class includes BL Lacertae objects (BL Lacs) and high polarization quasars (HPQs, which constitute a subset of flat-spectrum radio quasars, FS-RQs, characterized by high optical fractional polarization $> 3\%$; see Urry & Padovani 1995). In the framework of the ‘leptonic’ scenario for blazar emission, the radio-to-optical/X-ray segment of the emission continuum is due to synchrotron radiation of electron-positron pairs (e^\pm) accelerated up to \sim TeV energies, while the high-frequency X-ray-to- γ -ray segment is widely believed to be due to the inverse-Comptonization of various circum-nuclear photon fields (produced both internally and externally to the outflow) by the jet electrons (e.g., Ghisellini et al. 1998). Alternatively, in the ‘hadronic’ scenario, the high-energy emission continuum could also be generated via protons accelerated to ultra-high energies (\geq EeV), and producing γ -rays via either direct synchrotron emission or meson decay and synchrotron emission of secondaries from proton-photon interactions (e.g., Böttcher et al. 2013).

Blazars display strong flux variability at all wavelengths from radio to γ -rays, on time scales ranging from decades down to hours, or even minutes. The observed flux changes are often classified broadly into the three major types, namely ‘long-term variability’ (corresponding time scales of decades-to-months), ‘short-term variability’ (weeks-to-days), and intra-night/day variability (time scales less than a day; see, e.g., Wagner & Witzel 1995; Ulrich et al. 1997; Falomo et al. 2014). During the last decade, special attention has been paid to catching and characterizing large-amplitude and extremely rapid (minute/hour-long) flares in the γ -ray regime, with observed intensity changes of up to even a few orders of magnitude (Aharonian et al. 2007; Aleksić et al. 2011; Foschini et al. 2011; Saito et al. 2013; Rani et al. 2013; Ackermann et al. 2016). These are however rare, rather exceptional events, while, in general, the multiwavelength variability of blazar sources is of a ‘colored noise’ type, meaning larger variability amplitudes on longer variability timescales, with only low (percentage)-level flux changes on hourly timescales.

More precisely, the general shapes of the power spectral densities (PSDs) of blazar light curves, which may

Turkey

²¹ Physical Research Laboratory, Ahmedabad 380009, India

²² Astronomical Observatory of Taras Shevshenko National University of Kyiv, Observatorna str. 3, Kyiv, Ukraine

²³ IAC-NOT, C/Via Lactea, S/N, La Laguna E-38205, Spain

²⁴ Institute for Astronomy, Astrophysics, Space Applications and Remote Sensing, National Observatory of Athens, Metaxa & Vas. Pavlou St., Penteli, Athens, Greece

²⁵ BAA Variable Star Section, 5 Silver Lane, West Challow, Wantage, OX12 9TX, UK

²⁶ ICAMER Observatory of NASU 27 Acad. Zabolotnoho str. 03143, Kyiv, Ukraine

²⁷ Astronomical Observatory of National Ivan Franko University of Lviv, 8, Kyryla i Methodia str., 79005 Lviv, Ukraine

²⁸ C/Jaume Balmes No 24, E-08348 Cabriels, Barcelona, Spain

²⁹ C/.Riera, 1, B, Vallirana, E-0875, Barcelona, Spain

³⁰ Carretera de Martos 28 primero Fuensanta, Jaen 23001, Spain

³¹ Department of Physics and Astronomy, University of Delaware, Newark, DE 19716, USA

³² Institute of Astronomy and NAO, Bulgarian Academy of Science, 72 Tsarigradsko Chaussee Blvd., Sofia 1784, Bulgaria

³³ Department of Physics, Faculty of Science, Atatürk University, Erzurum 25240, Turkey

³⁴ Aritz Bidea No 8 4 B, E-48100 Mungia, Bizkaia, Spain

³⁵ Department of Astronomy, University of California, Berkeley, CA 94720-3411, USA

³⁶ Nordic Optical Telescope, Apartado 474, Santa Cruz de La Palma E-38700, Spain

³⁷ Muñas de Arriba La Vara, E-33780 Valdés, Spain

³⁸ C/Concejo de Teverga 9, 1 C, E-28053 Madrid, Spain

³⁹ Aryabhata Research Institute of Observational Sciences (ARIES), Nainital 263002, India

⁴⁰ Department of Physics and Astronomy, University of North Carolina, Chapel Hill, NC 27599, USA

⁴¹ Faculty of Science and Technology, University of the West Indies, St Augustine, Trinidad, West Indies

⁴² Astronomical Institute, The Czech Academy of Sciences, Ondřejov 25165, Czech Republic

⁴³ Czech Technical University, Faculty of Electrical Engineering, Prague 16627, Czech Republic

⁴⁴ Kazan Federal University, Kazan 420008, Russian Federation

⁴⁵ 16 Westminster Close, Basingstoke, Hampshire RG22 4PP, UK

⁴⁶ Planetary Plasma and Atmospheric Research Center, Tohoku University, Sendai 980-8578, Japan

⁴⁷ Department of Physics, University of Adiyaman, Adiyaman 02040, Turkey

⁴⁸ Isaac Newton Group of Telescopes, Apartado 321, Santa Cruz de La Palma E-38700, Spain

⁴⁹ Korea Astronomy and Space Science Institute, 776, Daedeokdae-Ro, Yuseong-Gu, Daejeon 305-348, Korea

⁵⁰ Partida de Maitino, Pol. 2 Num. 163, E-03206 Elche, Spain

⁵¹ Astrophysical Institute and University Observatory Friedrich Schiller University Jena, Schillergaesschen 2, D-07745 Jena, Germany

⁵² NF/Observatory, Silver City, NM 88041, USA

⁵³ INAF—Osservatorio Astronomico di Roma, via Frascati 33, Monteporzio Catone I-00040, Italy

⁵⁴ BAA Variable Star Section, 67 Ellerton Road, Kingstanding, Birmingham B44 0QE, UK

⁵⁵ Indian Institute of Astrophysics, II Block Koramangala, Bangalore 560 034, India

⁵⁶ Landessternwarte, Zentrum für Astronomie der Universität Heidelberg, Königstuhl 12, 69117, Heidelberg, Germany

⁵⁷ Observatori Cal Maciariol Mòdul 8. Masia Cal Maciariol,

Camí de l’Observatori s/n, E-25691 Ager, Spain

⁵⁸ Department of Astronomy & Astrophysics, Davey Lab, Pennsylvania State University, PA 16802, USA

⁵⁹ Astronomy and Space Physics Department, Taras Shevshenko National University of Kyiv, Volodymyrska str. 60, Kyiv, Ukraine

⁶⁰ Max Planck Institute for Extraterrestrial Physics, Giessenbachstrasse, Garching D-85748, Germany

⁶¹ Physik Department, Technische Universität München, James-Frank-Str., Garching D-85748, Germany

⁶² C/Petrarca 6 1^a E-41006 Sevilla, Spain

⁶³ C/Cardenal Vidal i Barraquee No 3, E-43850 Cambrils, Tarragona, Spain

⁶⁴ Instituto Nacional de Astrofísica, Óptica y Electrónica, Apartado Postal 51-216, Puebla 72000, México

⁶⁵ Florida International University and SARA Observatory, University Park Campus, Miami, FL 33199, USA

⁶⁶ Kiepenheuer-Institut für Sonnenphysik, Freiburg D-79104, Germany

⁶⁷ Janusz Gil Institute of Astronomy, University of Zielona Góra, Szafrana 2, Zielona Góra PL-65-516, Poland

⁶⁸ Department of Theoretical Physics and Astrophysics, Faculty of Science, Masaryk University, Kotlarska 2, 611 37 Brno, Czech Republic

typically be approximated to a first order by a single power-law $P(f) = Af^{-\beta}$, where f is the temporal frequency corresponding to the timescale $1/2\pi f$, A is the normalization constant, and $\beta > 0$ is the spectral slope, indicate that the observed flux changes observed in given photon energy ranges are correlated over temporal frequencies (Goyal et al. 2017, and references therein). So far, little or no evidence has been found for flattening of the blazar variability power spectra on the longest timescales covered by blazar monitoring programs (i.e., years and decades), even though such a flattening is expected in order to preserve the finite variance of the underlying (uncorrelated, by assumption) process triggering the variability (but see in this context Kastendieck et al. 2011; Sobolewska et al. 2014). Breaks in the PSD slope (from $0 < \beta < 2$ down to $\beta > 2$ at higher temporal frequencies) reported in a few cases may, on the other hand, hint at characteristic timescales related to either a preferred location of the blazar emission zone, the relevant particle cooling timescales, or some global relaxation timescales in the systems (Kataoka et al. 2001; Finke & Becker 2015; Sobolewska et al. 2014). The detection of such break features in blazar periodograms, would be therefore of a primary importance for constraining the physics of blazar jets. Due to observing constraints, however, the blazar light curves from ground-based observatories always sample limited temporal frequencies due to weather and visibility constraints. This issue is particularly severe at optical and very high-energy (VHE) γ -ray energies, where the timescales corresponding to $\sim 12 - 24$ hours can hardly be probed, in general. This difficulty has recently been surmounted in the optical range with the usage of *Kepler* satellite data, though only for rather limited numbers of blazars/AGN (Edelson et al. 2013; Revalski et al. 2014).

OJ 287 (J2000.0 R.A. = $08^{\text{h}}54^{\text{m}}48^{\text{s}}87$, Dec. = $+20^{\circ}06'36''64$; $z = 0.3056$; Nilsson et al. 2010), is a typical example of a ‘low-frequency-peaked’ BL Lac object with positive detection in GeV and TeV photon energy range (Abdo et al. 2010; O’Brien 2017). It is highly polarized in the optical band ($\text{PD}_{\text{opt}} > 3\%$; Wills et al. 2011), and exhibits a flat-spectrum radio core with a superluminal pc-scale radio jet, both characteristic of blazars (Wills et al. 1992; Lister et al. 2016). A supermassive black hole binary was claimed in the system, based on the evidence for a ~ 12 yr periodicity in its optical light curve (Sillanpaa et al. 1996; Valtonen et al. 2016); in addition, hints for a quasi-periodicity, with characteristic timescale of $\sim 400 - 800$ days, have been reported for the blazar based on the decade-long optical/NIR and high-energy γ -ray light curves (see, in the multiwavelength context Sandrinelli et al. 2016; Bhatta et al. 2016, for the most updated list of the claims of QPO detections in blazars, in general). OJ 287 is, in fact, one of the few blazars for which good-quality, long-duration optical monitoring data are available, dating back to circa 1896 (Hudec et al. 2013). It is also one of the few blazars which have been monitored by the *Kepler* satellite for a continuous monitoring duration of 72 days, with cadence becoming as small as 1 minute. Hence, OJ 287 is an outstanding candidate to characterize statistical properties of optical flux changes on the timescales ranging from ~ 100 years to minutes.

Here, for the first time, we present the optical PSD of OJ 287 covering — with no gaps — about six decades in temporal frequency, by combining the 117 year-long optical light curve of the source (using archival as well as newly acquired observations with daily sampling intervals), with the *Kepler* satellite data. The source has also been monitored in the radio (GHz) domain with a number of single-dish telescopes, in X-rays by the spaceborne *Swift*’s X-Ray Telescope (XRT), and in the high-energy γ -ray range with the Large Area Telescope (LAT) on board the *Fermi* satellite. Here we utilize these massive data set to derive the radio, X-ray, and γ -ray PSDs of OJ 287, and compare them with the optical PSD.

In Section 2 we describe in more detail all the gathered data, and the data reduction procedures. The data analysis and the results are given in Sections 3 and 4, respectively, while a discussion and our main conclusions are presented in Section 5.

2. DATA ACQUISITION AND ANALYSIS: MULTIFREQUENCY LIGHT CURVES

2.1. High energy γ -rays: *Fermi*-LAT

We have analyzed the *Fermi*-LAT (Atwood et al. 2009) data for the field containing OJ 287 from 2008 August 4 until 2017 February 6, and produced a source light curve between 0.1 and 300 GeV with an integration time of seven days. We have performed the unbinned likelihood analysis using Fermi ScienceTools 10R0P5 with P8R2_SOURCE_V6 source event selection and instrument response function, diffuse models GLL_IEM_V06.FITS and ISO_P8R22_SOURCE_V6_V06.TXT, for the 20° region centered at the blazar, following the Fermi tutorial⁶⁹. The procedure starts with the selection of good data and time intervals (using the tasks ‘GTSELECT’ and ‘GTMKTIME’ with selection cuts EVCLASS=128 EVTYPE=3), followed by the creation of an exposure map in the region of interest (ROI) with 30° radius for each time bin (tasks ‘GTLTCUBE’ and ‘GTEXPMAP’, while counting photons within zenith angle $< 90^{\circ}$).

We then computed the diffuse source response (task ‘GTDIFRSP’), and finally modeled the data with the maximum-likelihood method (task ‘GTLIKE’). In this last step, we used a model that includes OJ 287 and 158 other point sources inside the ROI (according to the third Fermi Large Area Telescope source catalog, 3FGL; Ackermann et al. 2015), in addition to the diffuse emission from our Galaxy and the extragalactic γ -ray background⁷⁰ (Acero et al. 2016). In the modeling, we followed the standard method and fixed the spectral indices and fluxes of all the point sources within the ROI other than the target at their 3FGL values. The γ -ray spectrum of OJ 287 was modeled with a log-parabola function. We considered a successful detection when the test statistic $\text{TS} \geq 10$, which corresponds to a signal-to-noise ratio of about $\geq 3\sigma$ (Abdo et al. 2009).

2.2. X-rays: *Swift*-XRT

We have analyzed the archival data from the *Swift*-XRT (Gehrels et al. 2004), consisting of a number of pointed observations made between 2005 May 20 and 2016 June 13. We used the latest version of calibration

⁶⁹ <http://fermi.gsfc.nasa.gov/ssc/data/analysis/scitools/>
⁷⁰ GLL_IEM_V06.FITS and ISO_P8R2_SOURCE_V6_V06.TXT

Table 1
Optical observations of OJ 287 made from ground-based observatories, and included in the present work

Data base (1)	Monitoring epoch (2)	Filter (3)	N (4)	Reference (5)
Harvard College Observatory ^(a)	1900 October 4 – 1988 November 16	B	272	Hudec et al. (2013)
Sonneberg Observatory	1930 December 20 – 1971 May 25	V	91	Valtonen & Sillanpää (2011)
Partly historical ^(b)	1971 March 25 – 2001 December 29	R	3717	Takalo (1994), this work
Catalina sky survey ^(c)	2005 September 4 – 2013 March 16	V	606	this work
Perugia and Rome data base	1994 June 3 – 2001 November 5	R	802	Massaro et al. (2003)
Shanghai Astronomical Observatory	1995 April 19 – 2001 December 29	R	71	Qian & Tao (2003)
Tuorla monitoring ^(d)	2002 December 7 – 2011 April 14	R	1525	Villforth et al. (2010), this work
Krakow quasar monitoring ^(e)	2006 September 19 – 2017 February 20	R	1155	Bhatta et al. (2016), this work

Columns: (1) Name of the observatory/university/monitoring programme; (2) period covered by the monitoring programme (start – end); (3) observing filter; (4) number of the collected data points; (5) references for the data (either full or partial data sets).

^(a)B-band measurements listed in Hudec et al. (2013), after applying quality cuts and removing the upper limits;

^(b)partly displayed in Figure 3a–c of Takalo (1994), converted to R-band by using a constant color difference;

^(c)<http://www.lpl.arizona.edu/css/>

^(d)<http://users.utu.fi/kani/1m/>

^(e)<http://www.as.up.krakow.pl/sz/oj287.html>

database (CALDB) and version 6.19 of the HEASOFT package⁷¹. For each data set, we used the level 2 cleaned event files of the ‘photon counting’ (PC) data acquisition mode generated using the standard XRPIPELINE tool.

The source and background light curve and spectra were generated using a circular aperture with appropriate region sizes and grade filtering using the XSELECT tool. The source spectra were extracted using an aperture radius of 47'' around the source position, while a source-free region of 118'' radius was used to estimate the background spectrum. The ancillary response matrix was generated using the task XRTMKARF for the exposure map generated by XRTEXPOMAP. All the source spectra were then binned over for 20 points and corrected for the background using the task GRPPHA. In none of the observations did the source count-rate exceed the recommended pile-up limit for the PC mode. For each exposure, we used routines from the X-ray data analysis software FTOOLS and XSPEC to calculate and to subtract an X-ray background model from the data. Spectral analysis was performed between 0.3 and 10 keV by fitting a simple power-law moderated by the Galactic absorption with the corresponding neutral hydrogen column density fixed to $N_{\text{H,Gal}} = 2.49 \times 10^{20} \text{ cm}^{-2}$ (the task NH in XSPEC). We used the unabsorbed 0.3–10 keV fluxes of OJ 287 obtained in this fashion to construct the source light curve.

2.3. Optical: ground-based telescopes and Kepler

The long-term optical data presented in this work have been gathered from several sources and monitoring programs listed in Table 1, including newly acquired measurements, together resulting in a *very long* optical light curve ranging from 1900 to 2017 February. We note that, starting from 2015 September 02, the blazar OJ 287 has been a target of a dense multiwavelength optical monitoring campaign ‘OJ287-15/16 Collaboration’ led by S. Zola, which was undertaken because of the predicted giant outburst in the system related to the ~ 12 -year-long periodicity of a putative supermassive black hole

binary (see, Valtonen et al. 2016; Sillanpää et al. 1996, and references therein). All the data taken from the start of 2016 through 2017 February used the skynet robotic telescope network⁷² and the Mt. Suhora telescopes, with external observers from Greece, Ukraine, and Spain (see Zola et al. 2016). For these newly acquired optical data, including also the Kraków quasar monitoring programme⁷³, the data reduction was carried out using the standard procedure in the Image Reduction and Analysis Facility (IRAF)⁷⁴ software package.

The procedure starts with pre-processing of the images through bias subtraction, flat-fielding, and cosmic-ray removal. The instrumental magnitudes of OJ 287 and the standard calibration stars listed in Fiorucci & Tosti (1996) in the image frames were determined by the aperture photometry using APPHOT. This calibration was then used to transform the instrumental magnitude of OJ 287 to a standard photometric system. Our data have quoted photometric uncertainties of $\sim 2 - 5\%$, arising mainly from large calibration errors in the estimated magnitudes of the stars in the field (Fiorucci & Tosti 1996). A typical 0.2 magnitude calibration uncertainty is assumed for B-band photographic magnitudes listed in Hudec et al. (2013). All the data were then averaged with one-day binning intervals. For the flux measurements obtained in B and V filters, fixed color differences of $B - R = 0.87$ and $V - R = 0.47$ were used to convert them to photometric R-band magnitudes in the standard Landolt photometric system (Takalo et al. 1994). Finally, for a given R-band magnitude M_R the R-band flux was derived as $3064 \text{ Jy} \times 10^{-0.4 \times M_R}$, where 3064 Jy is the zero point magnitude flux of the photometric system (Glass 1999); the errors in R-band fluxes were derived using standard error propagation (Bevington & Robinson 2003). The resulting long-term R-band historical light curve of OJ 287 is presented in Figure 1.

OJ287 was also observed during Campaign 5 (2015 April 27 – 2015 July 11) of the *Kepler*’s ecliptic second-life (K2) mission. The *Kepler* spacecraft contains a 0.95-

⁷² <http://skynet.unc.edu>

⁷³ <http://stach.ou.uj.edu.pl/kwazary/>

⁷⁴ <http://iraf.noao.edu/>

⁷¹ <http://heasarc.gsfc.nasa.gov/docs/software/lheasoft/>

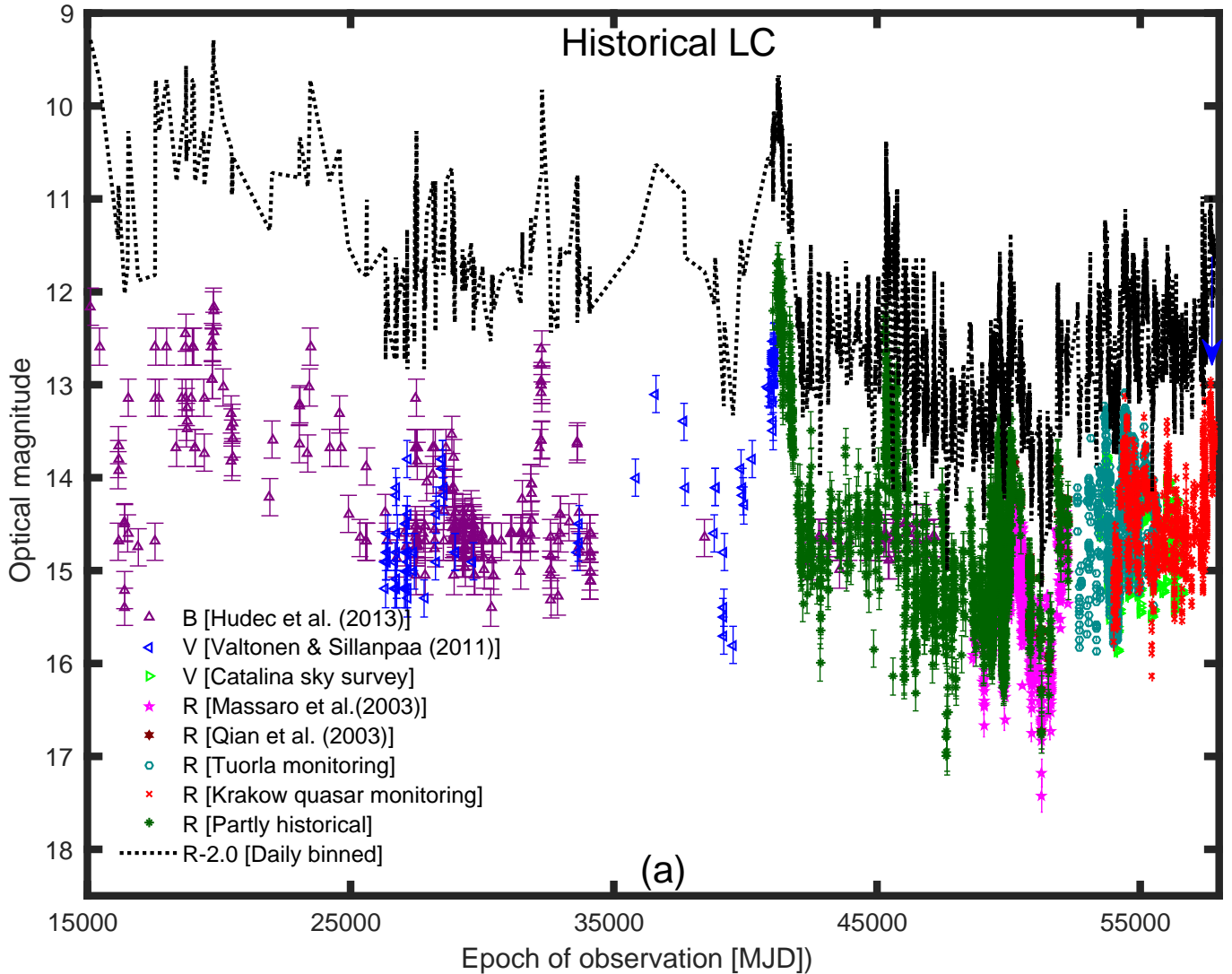


Figure 1. The long-term optical light curves of OJ 287 (X-axis ranges from 1899 December 12 until 2017 September 04), including the historical and also newly acquired measurements (see Section 2.3). The various symbols denote the original data for the given filter used in the observations. Blue arrow indicates the maximum of the giant outburst obtained in 2015 (2015 December 04; Valtonen et al. 2016) and the black dotted line traces the corresponding R-band luminosity evolution assuming fixed color differences, and it has been shifted vertically by two magnitudes for clarity.

m Schmidt telescope with a 110 square degree field of view imager with a pixel size of $4''$. It is in a heliocentric orbit currently about 0.5 AU from the Earth and provides high-cadence, very-high precision (1 part in 10^5) photometry for rather bright stellar targets (Howell et al. 2014). Campaign 5 lasted for 72 days, starting on 2015 April 27 and ending on 2015 July 10, data accumulating in both long (29.4 min) and short (58.85 sec) cadences. The data are publicly available from the Barbara A. Mikulski Archive for Space Telescopes (MAST) and stored in a fits table format⁷⁵. Timestamps are provided in Barycentric Julian Date (BJD). The long and short cadence data are not independent and that is why we used only the latter which provide higher temporal resolution. In the short cadence mode, for each timestamp a target mask is provided, while an optimal aperture is not, meaning that that the light curves are not extracted. To estimate the fluxes and their errors we applied our customized scripts

based on the tasks DAOFIND and PHOT in IRAF. We applied an aperture with a radius of 4 pixels. The background has been already subtracted during the in-house processing. The extracted light curve was subject to 4σ clipping. The errors were estimated following the recipe given in the PHOT manual.

K2 data analysis must struggle with on-board systematics. The most significant is the ‘thruster-firings’ which causes targets to drift across detector pixels; in addition, some temperature dependency can also be present. The former systematic can be accounted for, though in doing so, some intrinsic low frequency variability could be removed. Therefore, the thruster-firings need only be of concern if they mask the intrinsic variability present in the light curve. In our case the thruster firings are negligible and we have decided not to correct for them. Hence we assume that the K2 light curve found in this way is dominated by the intrinsic variability. Although some influence from temperature changes can still be present in the light curve, this systematic could not be accounted

⁷⁵ <https://archive.stsci.edu/k2/>

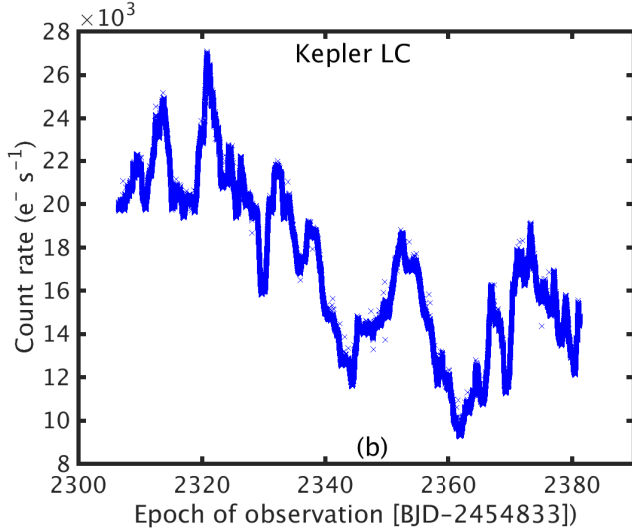


Figure 2. The optical light curve of OJ 287 (X-axis ranges from 2015 April 21 until 2015 July 30) from the *Kepler* satellite data analyzed in this paper (see Section 2.3); the errors are smaller than the point size in the figure.

for due to the lack of calibration files provided by the archive. The K2 short cadence light curve of OJ 287 is shown in Figure 2.

2.4. Radio frequencies: UMRAO and OVRO

The radio data were obtained from the University of Michigan Radio Astronomy Observatory (UMRAO) 26m dish at 4.8, 8.0, and 14.5 GHz, and the 40-m Telescope at the Owens Valley Radio Observatory (OVRO) at 15 GHz. The UMRAO fluxes at 4.8, 8.0, and 14.5 GHz were typically measured weekly (Aller et al. 1985), from 1979 March 23 to 2012 June 15, from 1971 January 27 to 2012 May 16, and from 1974 June 20 to 2012 June 23, respectively. The OVRO light curve at 15 GHz was sampled twice a week (Richards et al. 2011), during the period from 2008 January 8 to 2016 November 11. Discussions of the corresponding observing strategies and calibration procedures can be found in Aller et al. (1985) for the UMRAO data, and in Richards et al. (2011) for the OVRO data. Figure 3 (bottom panel) shows the resulting long-term radio light curves of OJ 287, compared with the high energy γ -ray, X-ray, and optical R-band light curves for the overlapping monitoring epochs. The zoomed-in version of the plot is shown in Figure 4, to highlight the *Swift*-XRT and *Fermi*-LAT data.

3. POWER SPECTRAL DENSITY ANALYSIS: CARMA

Power spectral analysis of astrophysical sources typically invokes Fourier decomposition methods, where a source light curve is represented by a sum of a set of sinusoidal signals with random phases, which correspond to various timescales of a source’s variability in the time series (e.g., Timmer & Koenig 1995). As such, the constructed PSD is a Fourier transform without the phase information. However, PSDs generated using Fourier decomposition methods can be distorted due to *aliasing* and *red-noise leak*. Aliasing arises from the discrete sampling of a time series, while the red-noise leak appears because of the finite length of a light curve. This problem is particularly severe if a time series is not evenly

sampled, as the response of a spectral window (i.e., the discrete Fourier transform of the sampling times) is in such a case unknown in the Fourier domain (e.g., Deeming 1975). Therefore, in order to derive reliable PSDs, an evenly sampled time series has to be obtained through a linear interpolation from an unevenly sampled data. Even though this procedure introduces false data in a time series, the underlying PSD parameters can then be recovered up to a typical (mean) sampling interval of an unevenly sampled time series (see the discussion in Goyal et al. 2017, and in particular the Appendix therein).

Since our aim is to characterize the variability properties of OJ 287 over an *extremely broad* range in temporal frequencies (~ 6 decades), using the 117 yr-long optical light curve, albeit with extremely uneven sampling, instead of standard Fourier decomposition methods here we use a certain statistical model to fit the light curve in the time domain, and thus to derive the source power spectrum.⁷⁶ Specifically, we use the publicly available Continuous-time Auto-Regressive Moving Average (CARMA) model⁷⁷ by Kelly et al. (2014), which is a generalized version of the first-order Continuous-time Auto-Regressive (CAR(1)) model (also known as an Ornstein-Uhlenbeck process). In the CAR(1) model, the source variability is essentially described as a damped random walk, i.e. a *stochastic* process with an exponential co-variance function $S(\Delta t) = \sigma^2 \exp(-|\Delta t/\tau|)$ defined by the amplitude σ and the characteristic (relaxation) timescale τ (Kelly et al. 2009). Meanwhile, in the CARMA model, the measured time series $y(t)$ is approximated as a process defined to be the solution to the stochastic differential equation

$$\begin{aligned} & \frac{d^p y(t)}{dt^p} + \alpha_{p-1} \frac{d^{p-1} y(t)}{dt^{p-1}} + \dots + \alpha_0 y(t) \\ &= \beta_q \frac{d^q \epsilon(t)}{dt^q} + \beta_{q-1} \frac{d^{q-1} \epsilon(t)}{dt^{q-1}} + \dots + \epsilon(t), \end{aligned} \quad (1)$$

where $\epsilon(t)$ is the Gaussian (by assumption) “input” white noise with zero mean and variance σ^2 , the parameters $\alpha_0 \dots \alpha_{p-1}$ are the autoregressive coefficients, the parameters, $\beta_1 \dots \beta_q$ are the moving average coefficient, and finally $\alpha_p = 1$ and $\beta_0 = 1$. The case with $p = 1$ and $q = 0$ corresponds to the CAR(1) process; hence a CARMA(p, q) model describes a higher-order process when compared with CAR(1).

For an in-depth discussion on the CARMA model, the reader is referred to Kelly et al. (2014). Here we only note that in this approach, for a given light curve $y(t)$, one derives the probability distribution of the (stationary) CARMA(p, q) process via Bayesian inference, and in this way one calculates the corresponding power spectrum

$$P(f) = \sigma^2 \left| \sum_{j=0}^q \beta_j (2\pi i f)^j \right|^2 \left| \sum_{k=0}^p \alpha_k (2\pi i f)^k \right|^{-2}, \quad (2)$$

along with the uncertainties. Kelly et al. (2014) provides

⁷⁶ Note that for the sparsely sampled data for OJ 287 obtained before 1970, a linear interpolation would introduce linear trends on the timescales as long as several years, in conflict with stochastic flux changes observed on similar timescales in the much more regular monitoring conducted during the last decades.

⁷⁷ <https://github.com/brandonckelly/carpack>

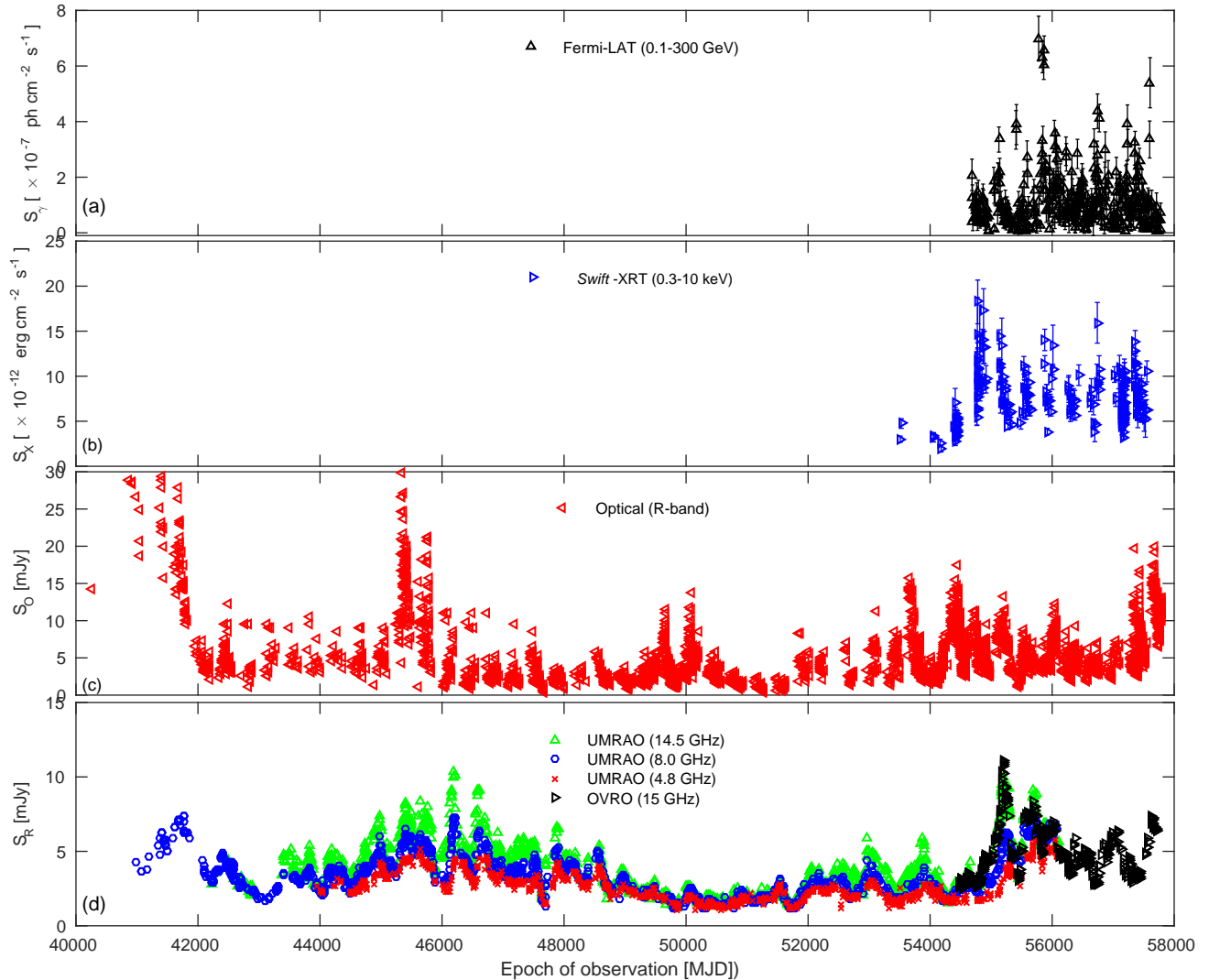


Figure 3. The multiwavelength, long-term light curves of OJ 287 for the monitoring epoch ranging from 1971 January until 2017 September. The X-axis ranges from 1958 May 24 until 2017 September 04. Panel (a) shows the *Fermi*-LAT light curve for the energy range 0.1–300 GeV. Panel (b) shows the *Swift*-XRT light curve at 0.3–10 keV energies. Panel (c) shows the optical R-band light curve. Panel (d) shows the 4.8–15 GHz radio light curves, as detailed in the panel legend. For clarity, the optical and radio flux measurements are shown without error bars, as the associated measurement uncertainties are smaller than the point size for >99.9% of the data points.

the adaptive Metropolis MCMC sampler routine to obtain the maximum likelihood estimates. The quality of the fit is assessed by standardized residuals: if the Gaussian CARMA model is correct, the residuals should form a Gaussian white noise sequence, for which the autocorrelation function (ACF) is normally distributed with mean zero and variance $1/N$, where N is the number of data points in the measured time series. Importantly, since a light curve is directly modeled in the time-domain, the ‘un-even sampling’ effects are automatically taken care of.

The order of CARMA(p, q) process is chosen using the generalized Akaike Information Criterion (hereafter AICc; Hurvich & Tsai 1989), which is based on the maximum likelihood estimate of the model parameters, including penalizing against overfitting due to the model complexity for finite sample sizes. In particular, models with the AICc values < 2 can be considered as sufficiently close to the null hypothesis, while models with the AICc values > 10 are not supported (Burnham &

Anderson 2004). The CARMA software package finds the maximum likelihood estimates of the model parameters by running 100 optimizers with random initial sets of model parameters, and then selects the order (p, q) that minimizes the AICc.

Finally, we note that the noise floor level in the derived PSD (equation 2) resulting from statistical fluctuations due to measurement errors, is calculated as

$$P_{stat} = 2 \Delta t \sigma_{stat}^2, \quad (3)$$

where Δt is the sampling interval and $\sigma_{stat}^2 = \sum_{j=1}^{j=N} \Delta y(t_j)^2 / N$ is the mean variance of the measurement uncertainties on the flux values $y(t_j)$ in the observed light curve at times t_j .

4. RESULTS

The flux distributions of blazar light curves can be modeled non-linearly, in the sense that they often can be represented as $y(t) = \exp[l(t)]$ where $l(t)$ is a lin-

Table 2
PSD parameters for the light curves of OJ 287

Data set	N	σ_{stat}^2 [rms ²]	$\Delta T_{\text{mean}}^\dagger$ [day]	$\Delta T_{\text{med}}^\ddagger$ [day]	T_{obs} [yr]	$\log(P_{\text{mean}})$ [rms ² day]	$\log(P_{\text{med}})$ [rms ² day]	$\log f_{br}$ [day ⁻¹]	$\log(f1)$ [day ⁻¹]	$\log(f2)$ [day ⁻¹]	β_1	β_2
(1)	(2)	(3)	(4)	(5)	(6)	(7)	(8)	(9)	(10)	(11)	(12)	(13)
<i>Fermi</i> -LAT ^a	327	$3.0 e^{-1}$	9.5	7.0	8.5	+0.76	+0.63	-2.3	-3.5 to -2.3	-2.8 to -1.8	0.0	1.0
<i>Swift</i> -XRT ^a	239	$2.3 e^{-2}$	18.2	2.9	11	-0.07	-0.86	-2.2	-3.6 to -2.9	-2.9 to -2.1	0.5	1.7
Optical (all) ^b	3490	$8.9 e^{-2}$	12.2	1.6	117	+0.33	-0.54	-	-4.6 to -1.4	-	1.2	-
Optical (trun.) ^b	3238	$1.5 e^{-2}$	5.2	1.5	46	-0.81	-1.37	-	-4.2 to -0.9	-	1.4	-
<i>Kepler</i> ^a	109408	$1.2 e^{-5}$	0.00068	0.00068	0.2	-7.78	-7.78	0.08	-1.9 to +0.08	+0.08 to +1.2	1.9	3.2
OVRO ^a	529	$5.1 e^{-4}$	6.1	3.2	5.1	-2.20	-2.48	-2.3	-3.5 to -2.3	-2.3 to -1.5	1.6	3.1
UMRAO ₁ ^a	1364	$8.8 e^{-4}$	10.2	6.0	33	-1.74	-1.97	-3.1	-4.1 to -3.1	-3.1 to -1.5	1.0	2.1
UMRAO ₂ ^a	1300	$9.0 e^{-4}$	11.6	7.0	41	-1.67	-1.89	-3.1	-4.2 to -3.1	-3.1 to -1.6	1.4	2.1
UMRAO ₃ ^a	978	$1.3 e^{-3}$	12.4	7.9	38	-1.49	-1.69	-2.8	-4.1 to -2.8	-2.8 to -1.9	1.5	2.4

Columns: (1) Data set; ^aPSD fitted with a broken power-law. ^b PSD fitted with a single power-law; in such a case, column (10) corresponds to the entire time range and column (12) gives the fitted slope. The subscripts 1,2 and 3 respectively, refer to the 14.5, 8.0, and 4.8 GHz observing frequencies for the UMRAO data sets. (2) number of data points in the observed light curve; (3) mean variance of the light curve due to measurement uncertainties; (4) mean sampling interval of the observed light curve (duration of the monitoring divided by the number of data points); (5) median sampling interval of the light curve; (6) total duration of the light curve; (7) mean noise floor level in the PSD due to measurement uncertainty (Eq. 3); (8) median noise floor level in the PSD due to measurement uncertainty (Eq. 3); (9) break frequency in case of the power spectrum fitted with a broken power-law; (10) temporal frequency range below the break covered by the spectral analysis, above the median noise floor level; (11) temporal frequency range above the break covered by the spectral analysis, above the median noise floor level; (12) power-law slope of the PSD below the break (corresponding errors are smaller than 0.05). (13) power-law slope of the PSD above the break (corresponding errors are smaller than 0.05).

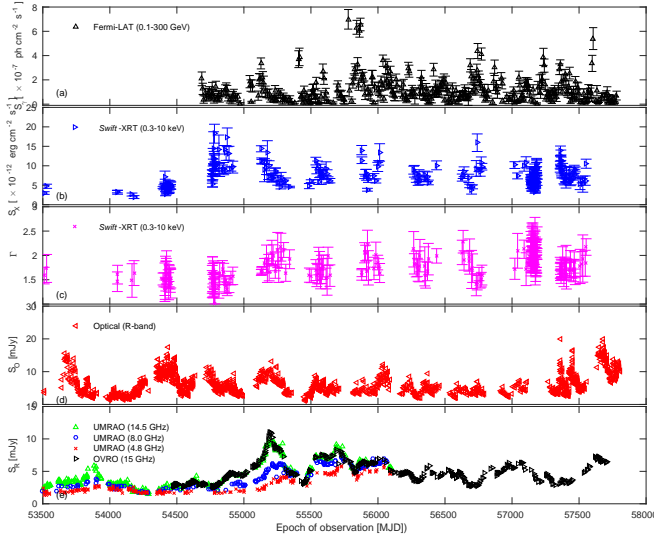


Figure 4. A zoomed-in version of Figure 3 along with a run of computed photon indices, Γ , for the *Swift*-XRT data (see Section 2.2), for the monitoring period from 2005 October until 2017 September. The X-axis ranges from 2005 May 10 until 2017 September 04.

ear Gaussian time-series (see, e.g., Edelson et al. 2013; Kushwaha et al. 2016; Abdalla et al. 2017; Liidakis et al. 2017). Hence we have logarithmically transformed the light curves of OJ 287 analyzed here (Figures 1–3), and then modeled them as Gaussian CARMA(p, q) processes. For each light curve, the minimum (p, q) order was selected by minimizing the AICc values on the grid $p = 1, \dots, 7$ and $q = 0, \dots, p - 1$. For such, we ran the MCMC sampler for \mathcal{N} iterations with the first $\mathcal{N}/2$ iterations discarded as a burn-in. Next, we employed the Gelman & Rubin (1992) method as a diagnostic to analyze the chain convergence using the multiple-chain approach, allowing to compare the “within chain” and “between-

chain” variances. The number of iterations was chosen to derive the potential scale reduction factor for all the model parameters to be less than 1.001. We select as the best-fit model that produced by the pair of p, q values having the lowest order within the range in which models are statistically indistinguishable from each other (i.e., minimum AICc < 10; see Section 3). Figure 15 in Appendix A shows, for comparison, the power spectra obtained for different p, q parameters consistent with the null hypothesis of the CARMA process for the analyzed *Fermi*-LAT light curve (see, Figure 3(a)).

The results of the CARMA model fitting are presented in Figures 5 (high-energy γ -rays), 6 (X-rays), 7–9 (optical), and 10–13 (radio). In these figures, we plot the measured time series along with the interpolated values based on the best-fit CARMA process (panels a), the standardized residuals and their distribution compared with the expected normal distributions (panels b), the corresponding ACFs (and the squared ACFs) compared with the 95% confidence regions for a white-noise process (panels c), the AICc values for different (p, q) pairs (panels d), and the resulting PSDs with 2σ confidence regions, as well as noise floor levels P_{stat} marked by horizontal lines (panels e). As shown, all the analyzed light curves are well represented by Gaussian CARMA processes, as the residuals from the model fitting follow the expected normal distributions with the ACFs and the squared ACFs lying within 2σ intervals for most of the temporal lags. Note that because some of the light curves are sparsely sampled (in particular, the historical optical and the *Swift*-XRT light curves), we estimated the noise floor level (equation 3) with either “mean” or “median” sampling intervals.

We also fitted the model PSDs with either a single power-law $P(f) \propto f^{-\beta}$, or a broken power-law $P(f) \propto (f/f_{br})^{-\beta_1, -\beta_2}$ where f_{br} is the break frequency and β_1 and β_2 are the slopes below and above the break, re-

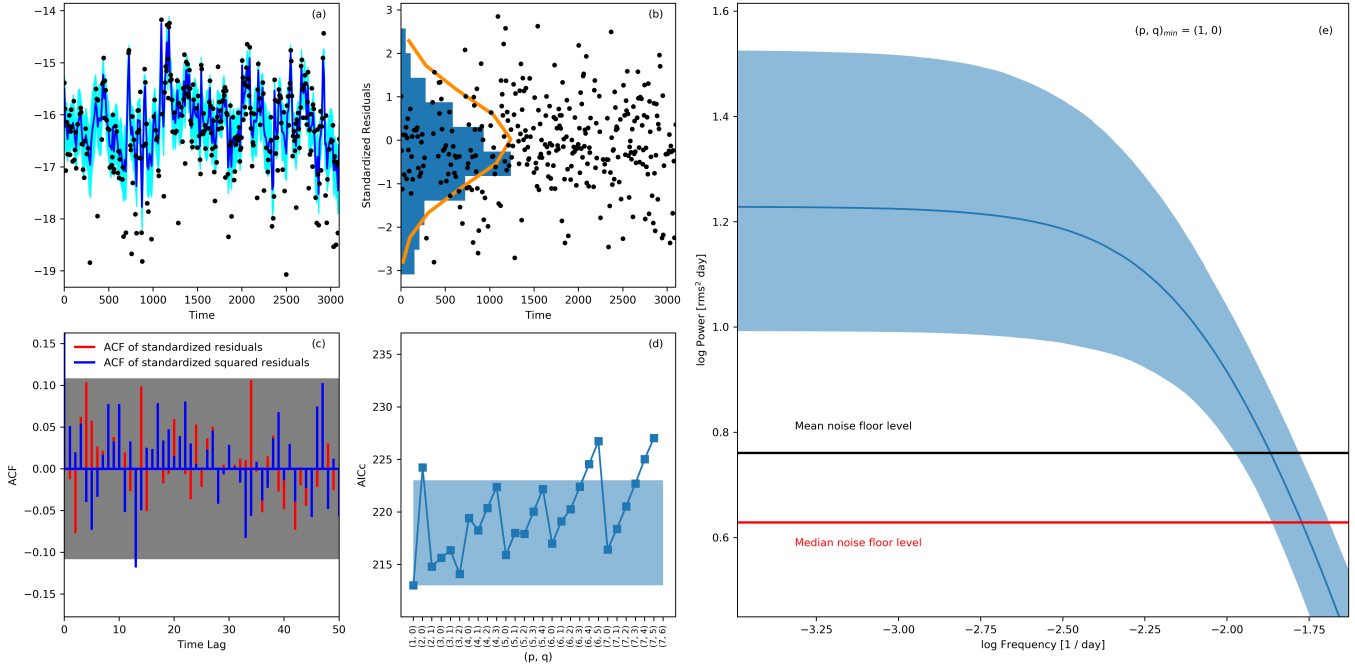


Figure 5. (a) The *Fermi*-LAT light curve of OJ 287 (black points), along with the interpolated values based on the best fitting CARMA(1,0) process selected according to the minimum AICc value (blue curve); (b) standardized residuals (black points) and their distribution (blue histogram) and compared with the expected normal distribution (orange curve); (c) the corresponding ACFs (red bars) and squared ACFs (blue bars), compared with the 95% confidence region assuming a white-noise process (grey shaded region); (d) the AICc values for various CARMA(p, q) models of the order $p \leq 7$ and $q < p$; the minimum AICc value is achieved for ($p = 1, q = 0$), but the blue shaded region denotes the models which are statistically indistinguishable; (e) the CARMA(1,0) model PSD of the *Fermi*-LAT light curve, along with the 2σ confidence region (blue area), as well as the mean and median noise floor levels (black and red lines, respectively).

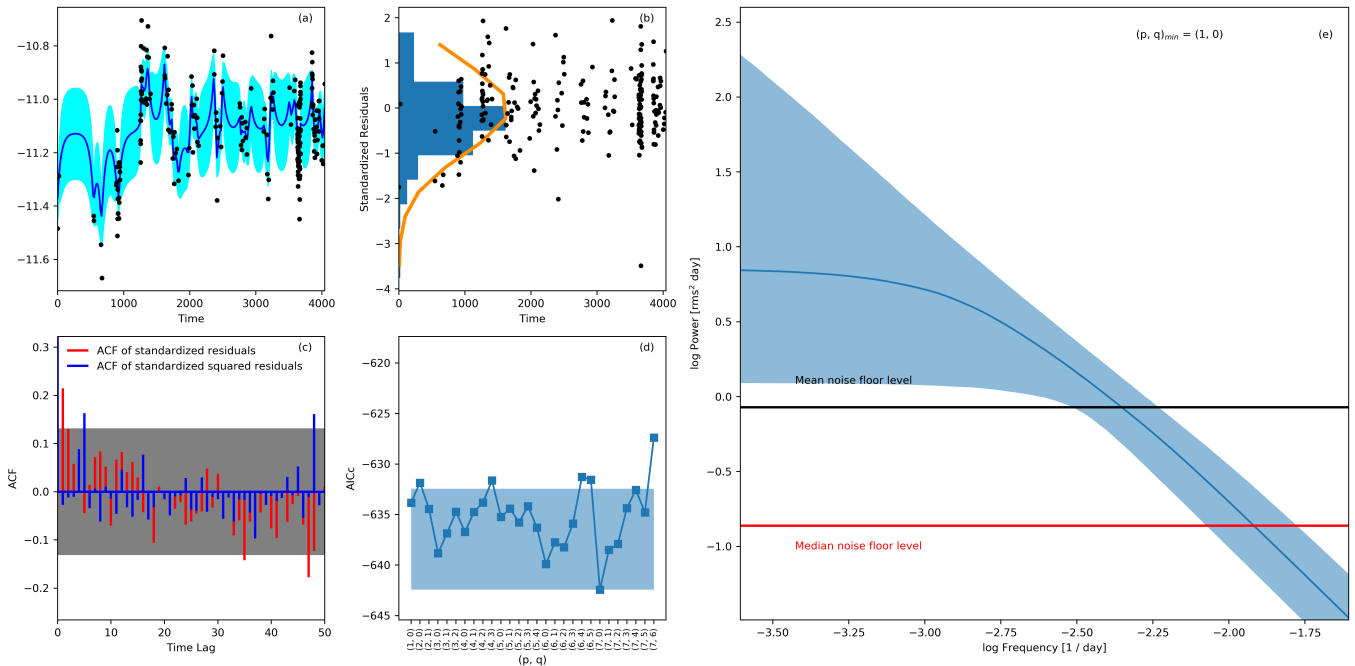


Figure 6. As in Figure 5, but for the *Swift*-XRT data, very well fit by the CARMA(1,0) model.

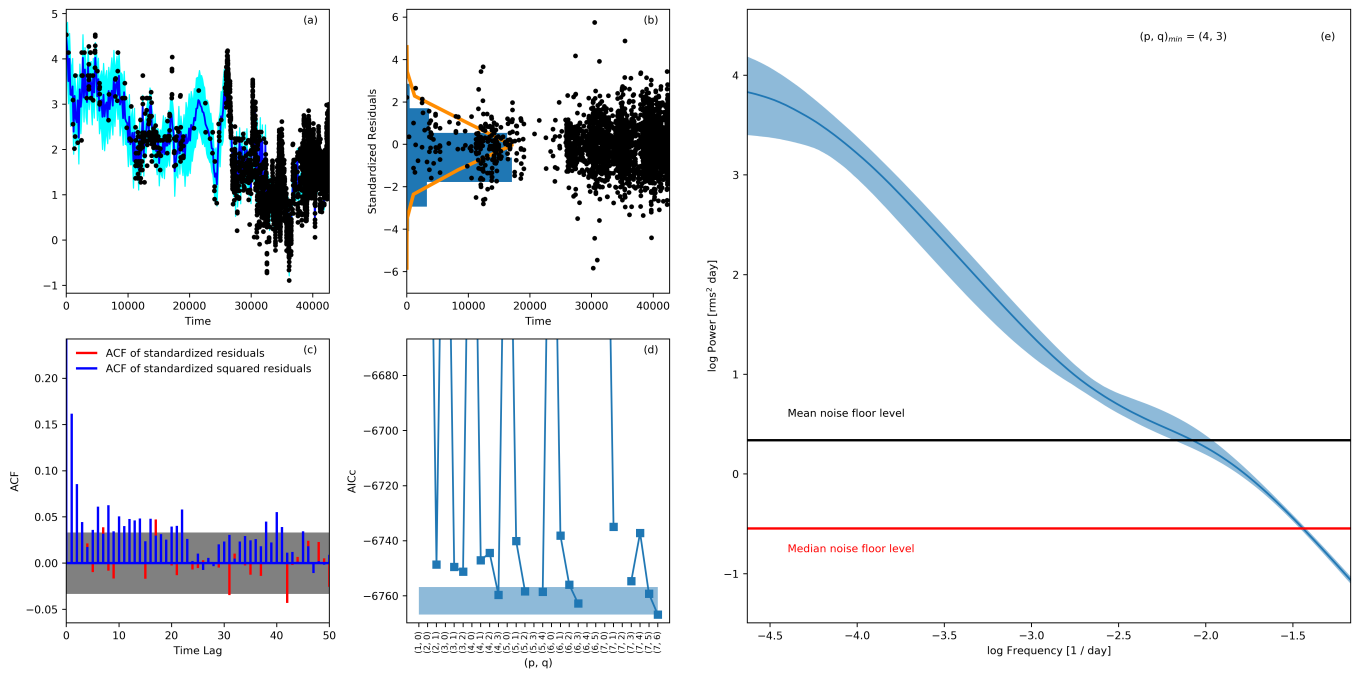


Figure 7. As in Figure 5, but for the entire optical data (optical (all); Table,2), very well fit by the CARMA(4,3) model.

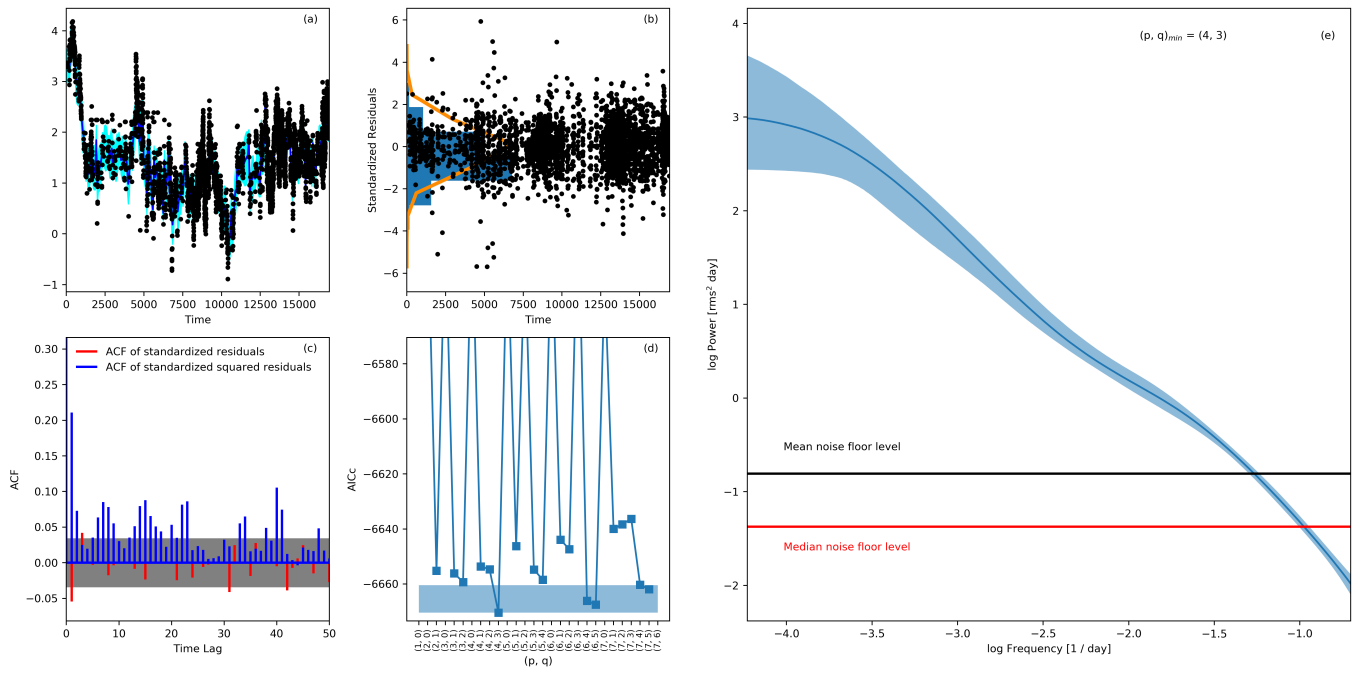


Figure 8. As in Figure 5, only for the historical 1970–2017 optical data (optical(trun.); Table 2), best fit by the CARMA(4,3) model.

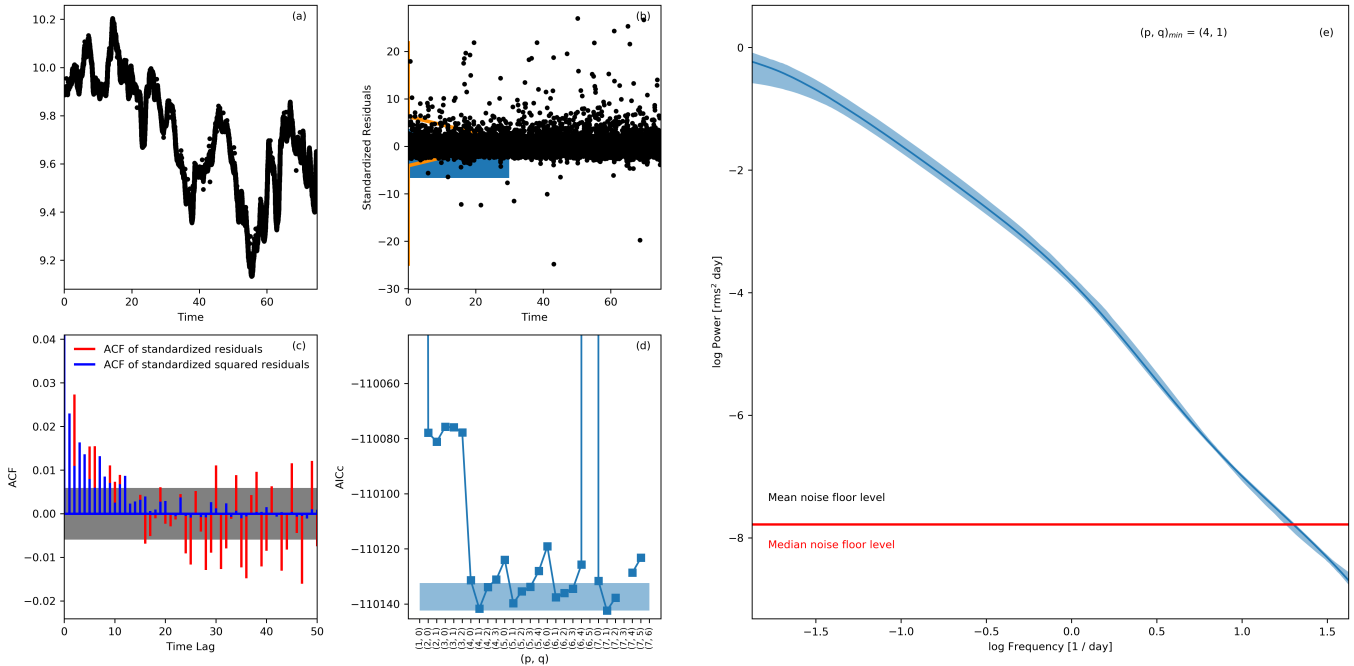


Figure 9. As in Figure 5, but for the *Kepler* data, very well fit by the CARMA(4, 1) model.

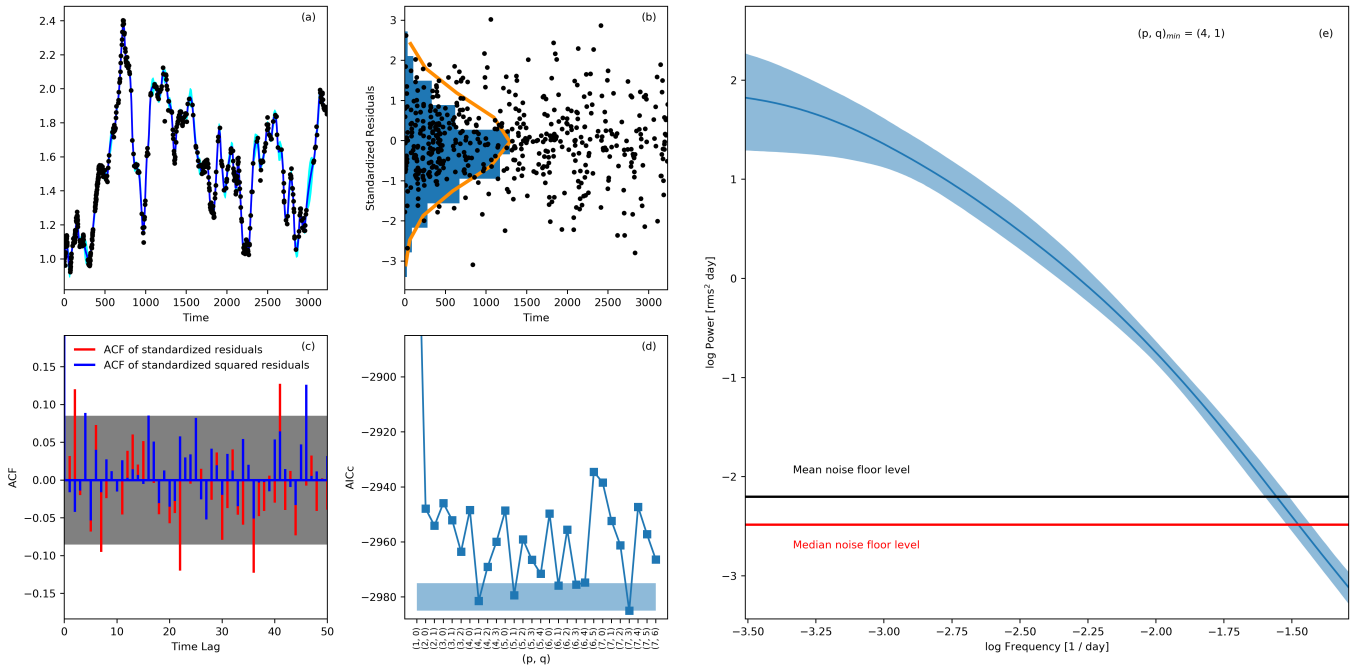


Figure 10. As in Figure 5, but for the 15 GHz OVRO data, best fitted by the CARMA(4, 1) model.

spectively, using linear regression with weighted error in log-log space above the median noise floor level; the results of the fitting, along with the errors calculated as the rms residuals between the model and the data, as well as the corresponding variability frequency ranges of the analyzed light curves, are summarized in Table 2.

Figure 7 presents the PSDs for the entire available long-term (1900–2017) monitoring optical data set, with typical daily sampling (hereafter “optical(all)”). The

majority of the optical data obtained before 1970 ($\sim 7\%$ of the data points) have measurement uncertainties of the order of 20%, due to large calibration errors resulting from observations recorded on photographic plates (see, Hudec et al. 2013 for discussion on error estimation). The overall noise floor level in the derived long-term PSD is relatively high, firstly due to larger measurement uncertainties and, secondly, because the mean sampling interval is large >12 days. Therefore, we also derived

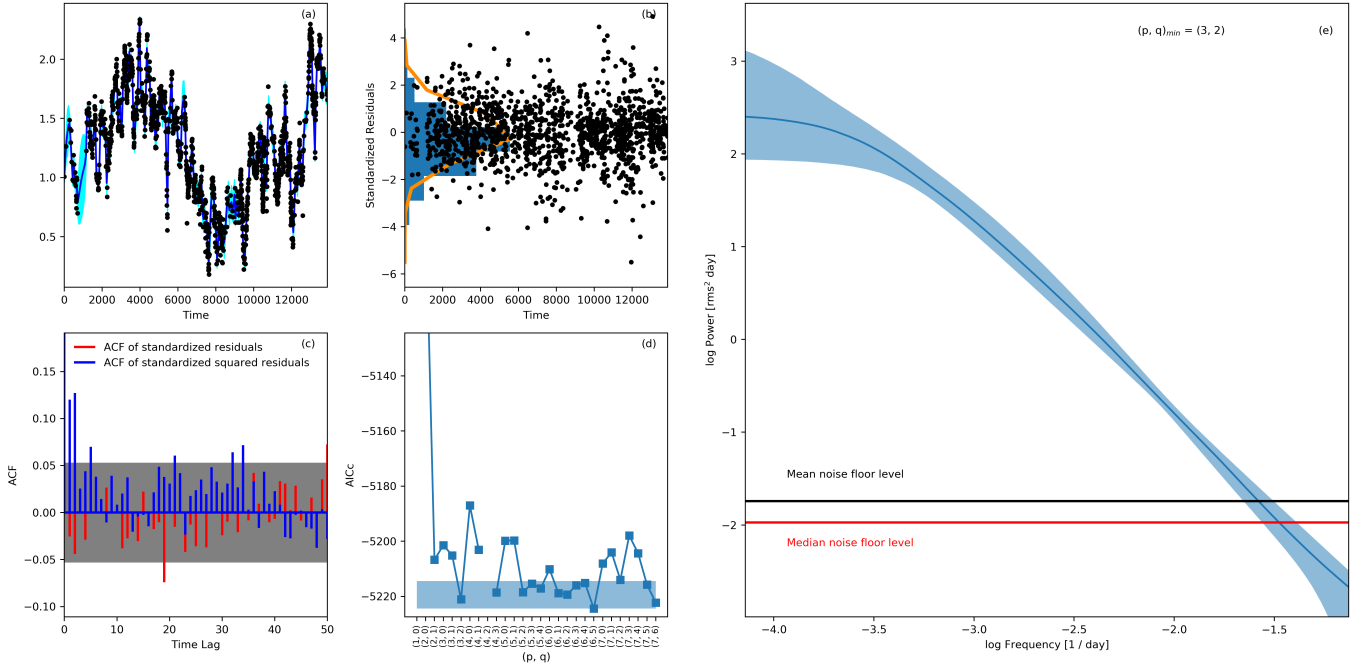


Figure 11. As in Figure 5, but for the 14.5 GHz UMRAO data, very well fit by the CARMA(3, 2) model.

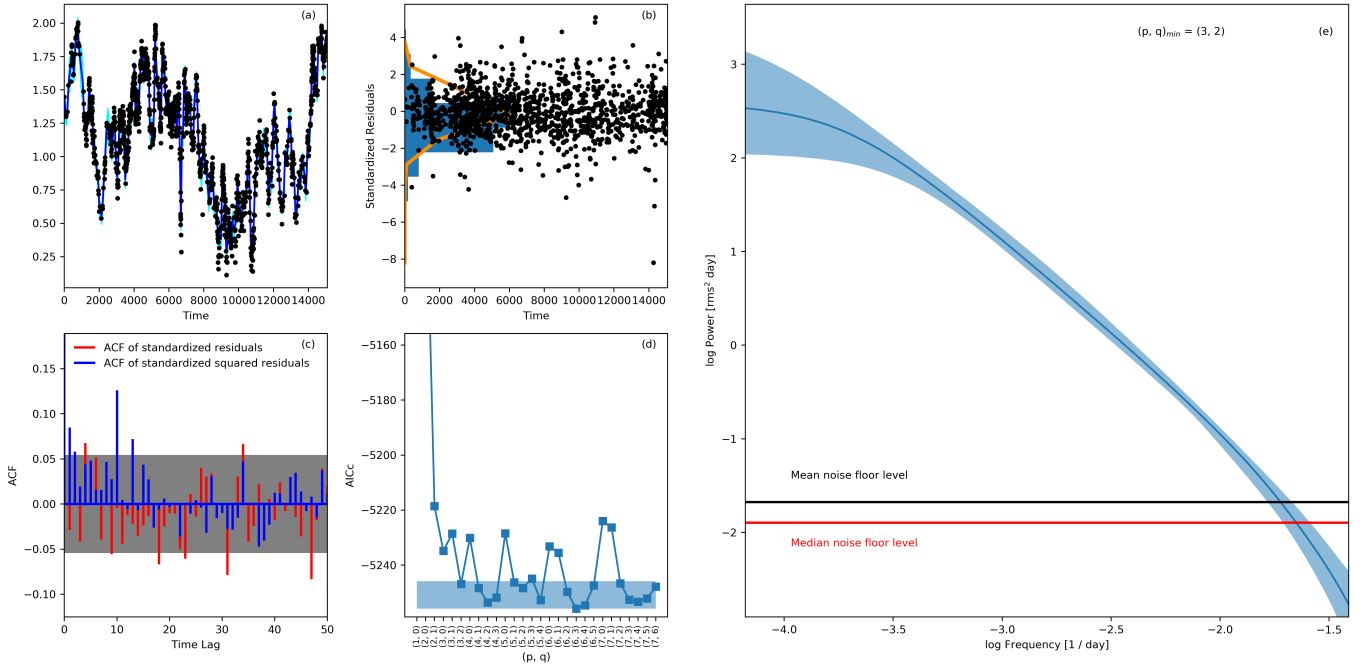


Figure 12. As in Figure 5, but for the 8 GHz UMRAO data, very well fit by the CARMA(3, 2) model.

the long-term PSD for the data obtained using only the good quality photo-multiplier tubes and CCD photometric measurements for the period 1970–2017, with typical measurement uncertainties $\sim 2 - 5\%$ and typical sampling of 5 days (hereafter “optical(trun.)”), as shown in Figure 8. Finally, the PSD corresponding to the continuous 72 day-long monitoring *Kepler* data, with sampling down to ~ 1 min (see Table 2), is presented in Figure 9. The optical PSD of the blazar obtained by combining the

PSDs generated with optical(all), optical(trun.), and the *Kepler* data, covers an unprecedented frequency range of nearly 6 dex (from 117 years down to hours timescales), *without* any gaps. The normalization of the *Kepler* PSD is found to be consistent with a simple extrapolation of the red-noise ($\beta \sim 1.4$) optical PSD from lower temporal frequencies.

Figure 14 presents the composite multiwavelength PSDs of OJ 287, truncated below the median noise floor

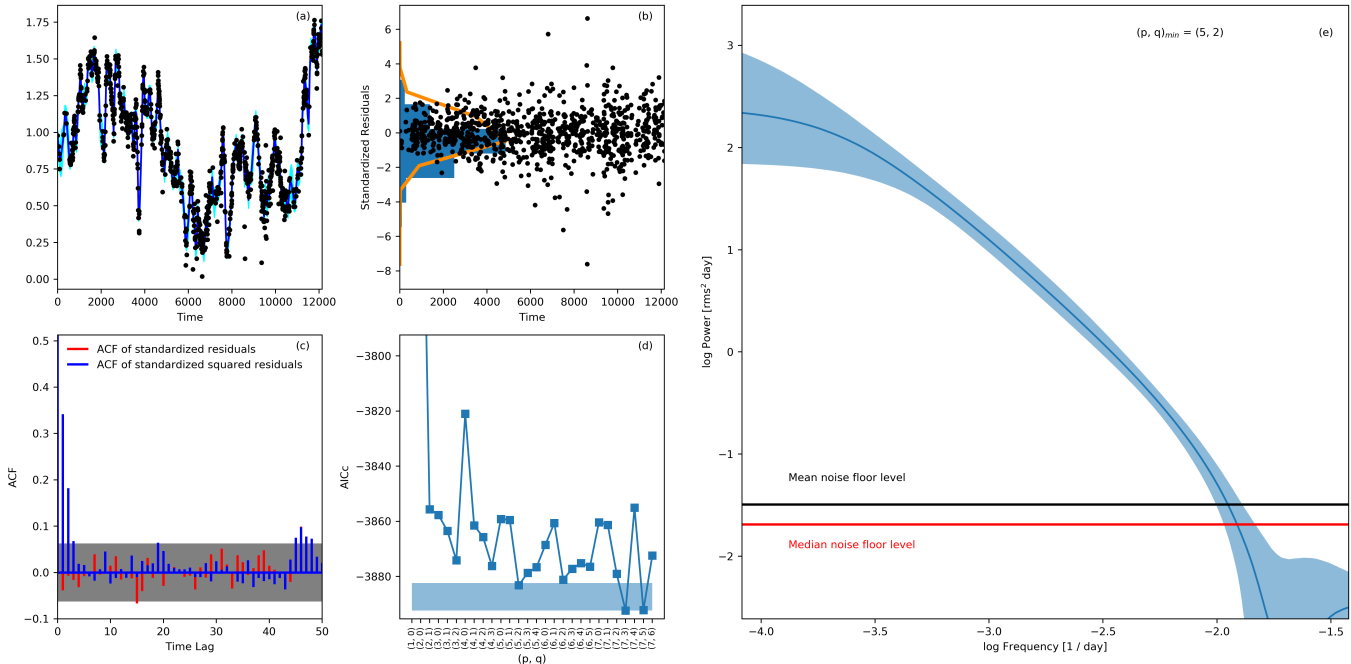


Figure 13. As in Figure 5, but for the 4.8 GHz UMRAO data, best fitted by the CARMA(5,2) model.

level for each data set. As seen, there is a remarkable similarity between the radio, optical, and X-ray bands (at least at longer, > 100 day timescales), and a clear difference between the high-energy γ -ray and lower-frequency bands over the timescales probed by the length of the light curves, down to the median sampling intervals.

5. DISCUSSION AND CONCLUSIONS

The main findings from our analysis of the multiwavelength and multi-epoch measurements of OJ 287 can be summarized as follows:

- i) On timescales ranging from tens of years down to months, the power spectra derived at radio frequencies indicate a red-noise character of the source variability (PSD slopes $\beta \simeq 1.2$ to 3; see Table 2) with a hint of a break on ~ 100 -1000 days.
- ii) Due to the inclusion of the *Kepler* data, we were able to construct *for the first time* the optical variability power spectrum of a blazar without any gaps across ~ 6 dex in temporal frequencies. The modeled power spectrum is well represented by a Gaussian CARMA process, revealing an approximately power-law form of the PSD roughly consistent with a red noise behavior, on the variability timescales ranging from 117 years down to sub-hours, with no hint for the presence of “quasi-periodic oscillations” (QPOs; see Figure 14 and Section 1).
- iii) A detailed comparison between the long-term optical monitoring data and the *Kepler* data, does indicate a break in the red noise-type optical power spectrum of OJ 287 (the corresponding PSD slopes $\beta \simeq 1.9 \pm 0.01$ and 3.2 ± 0.01 , respectively; see Figure 14), on the variability timescales of the order of about ~ 1 day.

iv) The power spectrum derived at X-ray photon energies based on the *Swift*-XRT data resembles the radio and optical power spectra ($\beta \simeq 0.5 - 1.7$) on the analogous timescales ranging from tens of years down to months with a hint of break on ~ 1000 days.

- v) The high-energy γ -ray power spectrum of OJ 287 modeled using the *Fermi*-LAT data, is noticeably different from the radio, optical, and X-ray power spectra of the source. In particular, we have detected the characteristic relaxation timescale in the *Fermi*-LAT data, corresponding to $\simeq 100^{+190}_{-60}$ days with a 3σ confidence interval limit (Figure 5): on timescales longer than 100 days, the PSD slope is consistent with $\beta = 0$ (white noise), while $\beta \simeq 1.0$ (pink/flickering noise) on shorter timescales. This timescale is also consistent with the corresponding break frequency obtained from the broken power-law fit within a 3σ confidence interval limit. In the framework of the Gaussian CARMA model, this power spectrum is consistent with the CAR(1) process, according to the minimum AICc criterion adopted in this study. Yet, the fitted slope above the break is not consistent with the power-law index of 2, which is expected for a pure random walk process (Kelly et al. 2009). This discrepancy can arise because other higher order CARMA models probed in the parameter space, $p = 7, q < p$, cannot be excluded with high statistical significance (wide shaded region shown in Figure 5d).

5.1. Periodicity in the long-term optical and *Fermi*-LAT light curves

OJ 287 has become famous to a large extent because of the claims of ~ 12 year periodicity in its optical light curve (see, e.g., Valtonen et al. 2016, for a recent review).

However, the present analysis does not reveal any well-defined peak in the power spectrum corresponding to this timescale (see Figure 7). On the other hand, even though the total duration of the optical light curve analyzed in this paper is ~ 117 years, the data obtained before 1990 are highly irregularly sampled (see, also, Hudec et al. 2013). The better sampled 1970–2017 light curve (see Figure 8) covers only ~ 3 of the claimed cycles, and as such is not sufficiently long to reveal any significant periodicity over the red-noise power spectrum (see the discussion in Vaughan et al. 2016, Appendix B and C here). We also do not see any QPOs in either *Fermi-LAT* or optical data around ~ 400 days, reported by Sandrinelli et al. (2016) and Bhatta et al. (2016). This may be due to either a marginal significance of a roughly year-like quasi-periodicity ($\sim 3\sigma$, as reported in the aforementioned studies), or the transitory nature of such features (see the analysis and the discussion in Bhatta et al. 2016).

5.2. Characteristic variability timescales

As noted above, a detailed comparison between the long-term optical monitoring data and the *Kepler* data indicate breaks in the optical power spectrum of OJ 287 (from $\beta \simeq 1.9$ to $\simeq 3.2$), on the variability timescales of the order of one day. Interestingly, a fairly similar break, on broadly analogous timescales, has been reported by Isobe et al. (2015) in the X-ray power spectrum of the blazar Mrk 421, based on a comparison between the *MAXI* and *ASCA* satellite data (see also Kataoka et al. 2001). This break may indicate either a non-stationarity of the variability process in the source on the timescale of the order of days and shorter, or – if persistent – it may signal some characteristic variability timescale in the system (in particular, the timescale below which there is a rapid decline in the variability power, although overall the variability process is still of approximately the red-noise type). Interestingly, the peak of the synchrotron component (in the spectral energy distribution representation) falls within the optical range for OJ 287 (hence classified as a ‘low-frequency-peaked’ BL Lac), and in the X-ray range for Mrk 421 (‘high-frequency-peaked’ BL Lac object). Radio and XRT data analysed here also shows a presence of a break on timescales ~ 100 – 1000 days.

Turning to the *Fermi-LAT* light curve of OJ 287, our CARMA modeling shows a clear break in the variability power spectrum, i.e., on the timescales longer than ~ 100 days we see an uncorrelated (white) noise, and on the shorter timescales a correlated (colored) noise. The 100 days timescale is therefore a characteristic relaxation timescale in the system, which is however related only to the production of high-energy γ -rays. We note that breaks on roughly similar timescales have been noted in the radio and X-ray power spectra of the blazar (see, Table 2), though not in the optical range (see Figure 14). However, unlike the *Fermi-LAT* power-spectrum, the breaks in radio and X-ray power spectra are consistent with non-stationarity of the variability generating process (i.e., change of slope from 1 to 2 around ~ 1000 days). On the other hand, analogous breaks have frequently been reported in the optical and X-ray power spectra of radio-quiet AGN, on the timescales of the order of 100–1,000 days, the timescales which seem to correlate with the black hole mass and the accretion rate in

the studied systems (McHardy et al. 2006; Kelly et al. 2009, 2011). In radio quiet AGN, the observed optical and X-ray emission originate within the accretion disk, and $\lesssim 1,000$ day timescales could be reconciled with the thermal timescales of the innermost parts of the disks; in blazar sources, the observed γ -ray fluxes are instead due to relativistic jets, and there is no obvious physical reason of ~ 100 day timescale, unless one assumes a strong, almost one-to-one coupling between the disk and the jet γ -ray variabilities (see the discussion in Goyal et al. 2017; O’Riordan et al. 2017). Interestingly, a similar feature of the high-energy γ -ray power spectra, breaking from white to colored noise, has been reported before by Sobolewska et al. (2014) in the *Fermi-LAT* light curves of the BL Lac objects PKS 2155–304 and 3C 66A, albeit on shorter timescales of about a month, and in the long-term optical monitoring data for PKS 2155–304 by Kastendieck et al. (2011) on a timescale of $\sim 1,000$ days.

5.3. Multiwavelength power spectra

In our recent analysis of the multiwavelength power spectra of the low-frequency-peaked BL Lac object PKS 0735+178, (Goyal et al. 2017), which however did not include any X-ray data, and was moreover based on the discrete Fourier transform method (with linear interpolation), we found that the statistical character of the γ -ray flux changes is different from that of the radio and optical flux changes. Specifically, the high-energy γ -ray power spectrum of the source was found to be consistent with a flickering noise, while the radio and optical power spectra with a pure red noise. There we suggested that this finding could be understood in terms of a model where the blazar synchrotron variability is generated by the underlying single stochastic process, and the inverse-Compton variability by a linear superposition of such processes, within a highly non-uniform portion of the outflow extending from the jet base up to the \lesssim pc-scale distances.

The more robust analysis of the much better quality multiwavelength data for OJ 287 presented in this paper, based on the CARMA modeling, to a large extent consistent with the findings reported before for PKS 0735+178 Goyal et al. (2017). That is, the overall slope of the high-energy γ -ray PSD in OJ 287 is significantly flatter than the slopes of radio or optical PSDs, and also the colored-noise type variability at optical frequencies occurs over a very broad range of variability timescales, from decades to hours. However, the new finding emerging from the analysis presented here is that (i) there may be a break in the red-noise optical power spectrum of OJ 287 on the timescale of about a day, (ii) the X-ray power spectrum of the source resembles the radio and optical power spectra on analogous timescales ranging from tens of years down to months, and that (iii) the high-energy γ -ray power spectrum of the blazar is of a pure flickering noise type, with the relaxation timescale of the order of 100 days (but not seen in the power spectra at lower photon energies).

The interpretation of the above novel findings is not straightforward, keeping in mind that, in the particular case of OJ 287, the observed X-ray emission seems to be mostly due to the inverse-Compton process involving the lowest-energy electrons, being only occasionally dominated by the high-energy tail of the synchrotron continuum (e.g., Seta et al. 2009). A possible resolution may

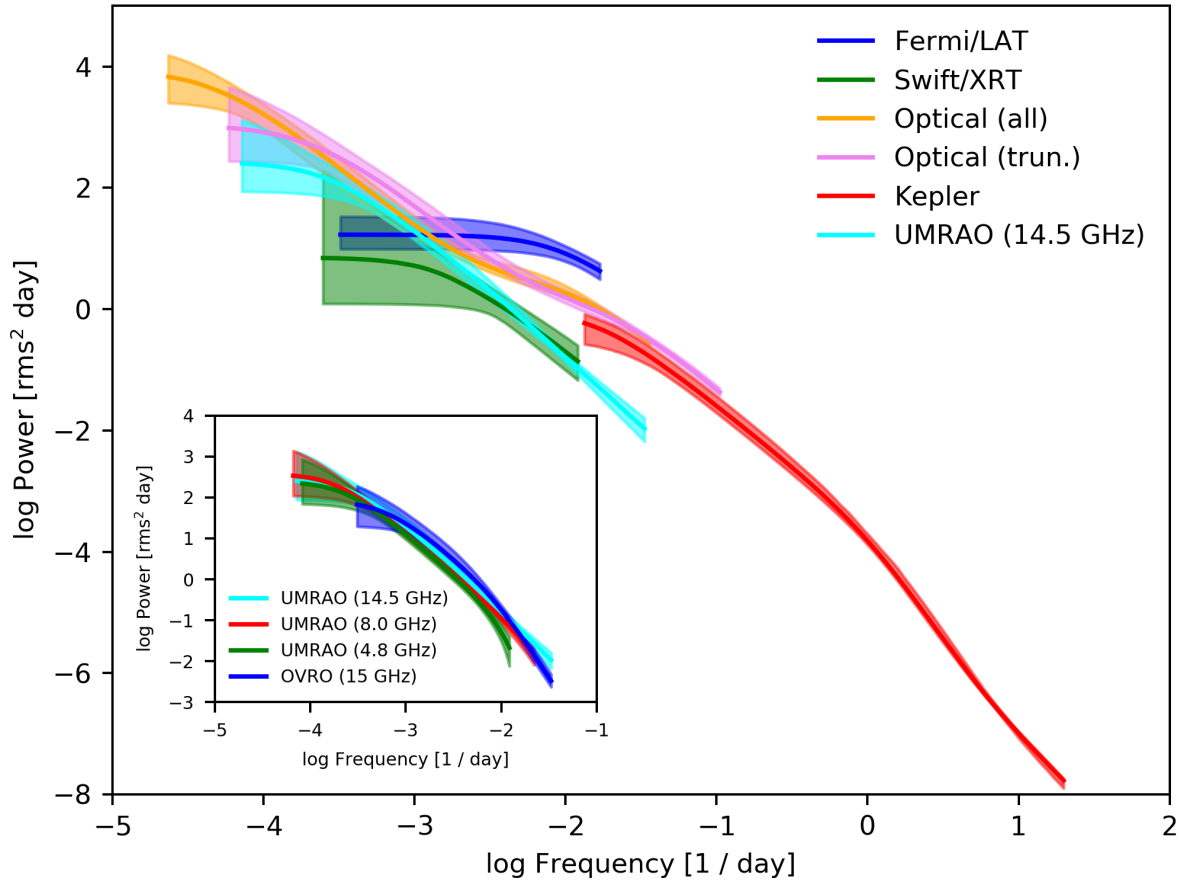


Figure 14. Composite multiwavelength power spectra of OJ 287, with the colored curves as described in the legend; 2σ confidence intervals are shown by the corresponding shaded regions.

lie in the scenario where the high-energy γ -ray emission does not constitute the high-energy tail of the broadband inverse-Compton continuum extending from X-ray photon energies, but instead is due to a distinct – spectrally and spatially – electron population, peaked at the highest electron energies, and distributed rather exclusively within the innermost parts of the jet, thus being much more responsive to the faster modulations associated with the accretion disk events as compared to the outer parts of the jet.

AG, MO, and VM acknowledge support from the Polish National Science Centre (NCN) through the grant 2012/04/A/ST9/00083. DKW and AG acknowledge the support from 2013/09/B/ST9/00026. LS is supported by Polish NSC grant UMO-2016/22/E/ST9/00061. MS acknowledges the support of 2012/07/B/ST9/04404. SZ acknowledges the support of 2013/09/B/ST9/00599. RH acknowledges GA CR grant 13-33324S. M. So. was supported by NASA contract NAS8-03060 (Chandra X-ray Center). M. So. also acknowledges the Polish NCN grant OPUS 2014/13/B/ST9/00570.

This research has made use of data from the University of Michigan Radio Astronomy Observatory which has been supported by the University of Michigan and by a series of grants from the National Science Foundation, most recently AST-0607523, and NASA Fermi grants NNX09AU16G, NNX10AP16G, and NNX11AO13G. The OVRO 40m Telescope Fermi Blazar Monitoring Program is supported by NASA under awards NNX08AW31G and NNX11A043G, and by the NSF under awards AST-0808050 and AST-1109911.

The Fermi-LAT Collaboration acknowledges support from a number of agencies and institutes for both development and the operation of the LAT as well as scientific data analysis. These include NASA and DOE in the United States, CEA/Irfu and IN2P3/CNRS in France, ASI and INFN in Italy, MEXT, KEK, and JAXA in Japan, and the K. A. Wallenberg Foundation, the Swedish Research Council, and the National Space Board in Sweden. Additional support from INAF in Italy and CNES in France for science analysis during the operations phase is also gratefully acknowledged.

APPENDIX

A. SELECTION OF p, q PARAMETER FOR THE CARMA PROCESS

The order of CARMA(p, q) process is chosen based on the of how close the model is to the data using the minimum AICc criterion adopted in the present study. It has been argued that the models for various pairs of p, q values for which the minimum AICc is within 10, are not statistically indistinguishable from each other. Figure 15 shows power spectra corresponding to few sets of p, q parameters of the analyzed *Fermi*-LAT light curve. We choose the lowest order model, i.e., CARMA(1,0), as a best fit model describing the high energy γ -ray variability in OJ287.

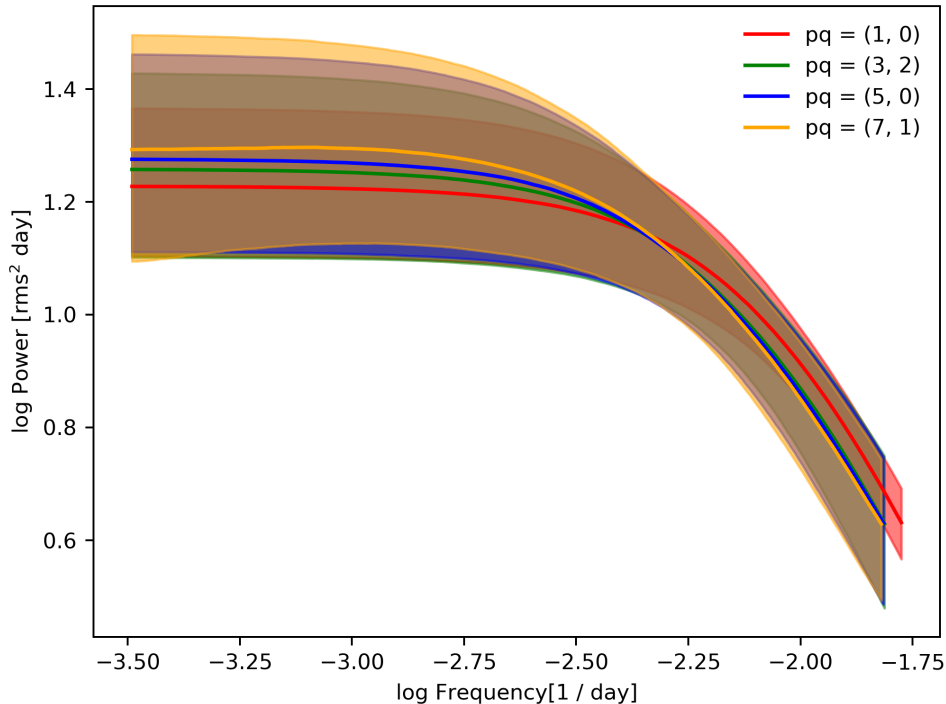


Figure 15. Power spectra corresponding to few sets of p, q parameters of the analysed *Fermi*-LAT light curve. The colored curves, as described in the legend, with 2σ confidence intervals are shown.

B. LACK OF ~ 12 YEAR QPO IN THE OPTICAL LIGHT CURVE

Here we discuss in more detail the lack of the claimed ~ 12 year near periodicity in the analyzed optical light curve. To demonstrate the robustness of the CARMA modeling in detecting QPO features against the background of red-noise in the power spectrum for a finite time series covering only a few periods, an artificial light curve is generated with three components, (1) a pure red-noise ($\beta = 2$) power spectrum using the method of Timmer & Koenig (1995), (2) a sinusoidal component with 12 year period, and (3) a Gaussian white noise with mean 0 and standard deviation 0.1 representing measurement uncertainty. The data points are evenly sampled with a sampling period of one day, and the total duration of the simulated time series is 14,600 days (=40 years, corresponding to our relatively better sampled optical light curve starting from 1970, see Table 2). Next, we keep 10% of the data selected at random times to mimic an unevenly sampled dataset. Figure 16(a-d) presents the results of CARMA modeling on our simulated light curve while Figure 16(e) presents the computed power spectrum. Since the simulated light curve covers only ~ 3 periods, we do not detect a clear peak on the ~ 12 year timescale against the background of red-noise power spectrum and a Gaussian white noise, in accordance with the discussion in Vaughan et al. (2016).

C. COMPARISON OF POWER SPECTRUM OBTAINED USING CARMA MODELING AND DFT USING HISTORICAL OPTICAL LIGHT CURVE (1900-2017)

We calculated the power spectrum using the DFT method for the optical(all) light curve analysed here (see, Goyal et al. 2017, for mathematical details on computing PSD using the DFT method). Figure 17 shows the resulting power spectrum obtained using CARMA modeling and the DFT method. Within 3σ confidence interval, the two methods give compatible results. A mild peak ~ 12 yr from the DFT method is within the 3σ confidence intervals estimated from the CARMA modeling.

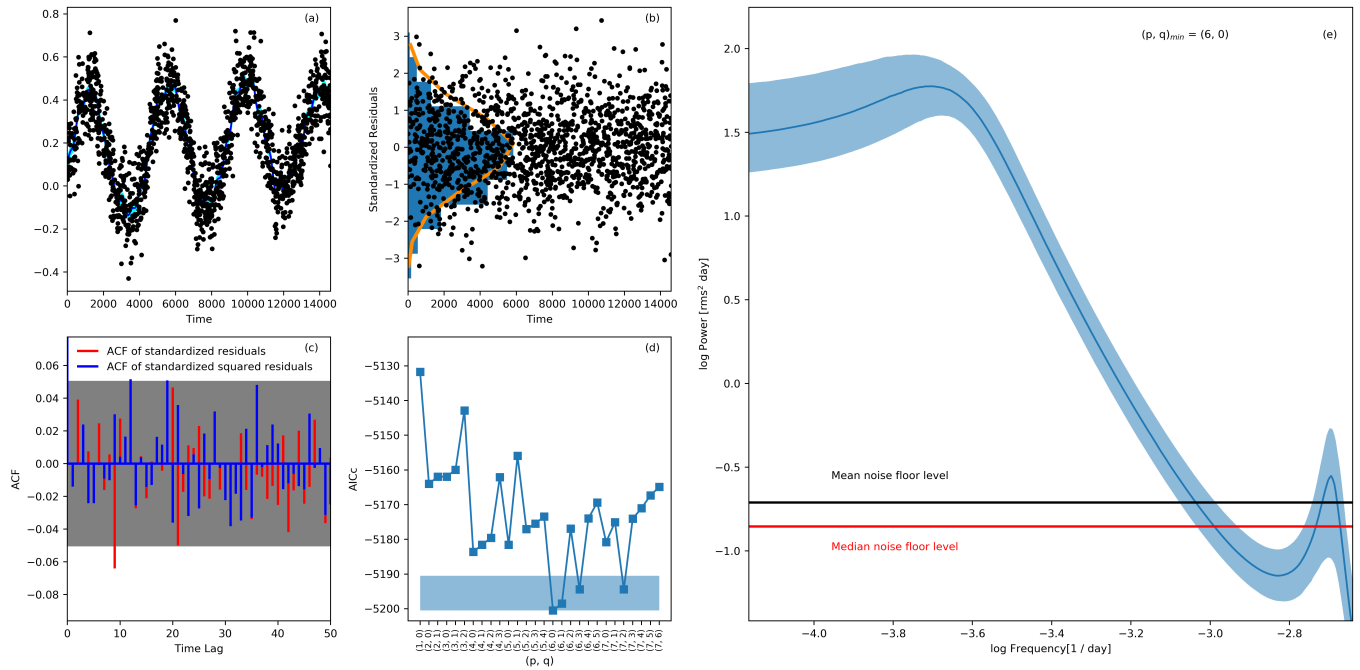


Figure 16. Result of CARMA modeling on the simulated light curve; the best-fit model is $p=6, q=0$ (the symbols and the legends are same as described in the text).

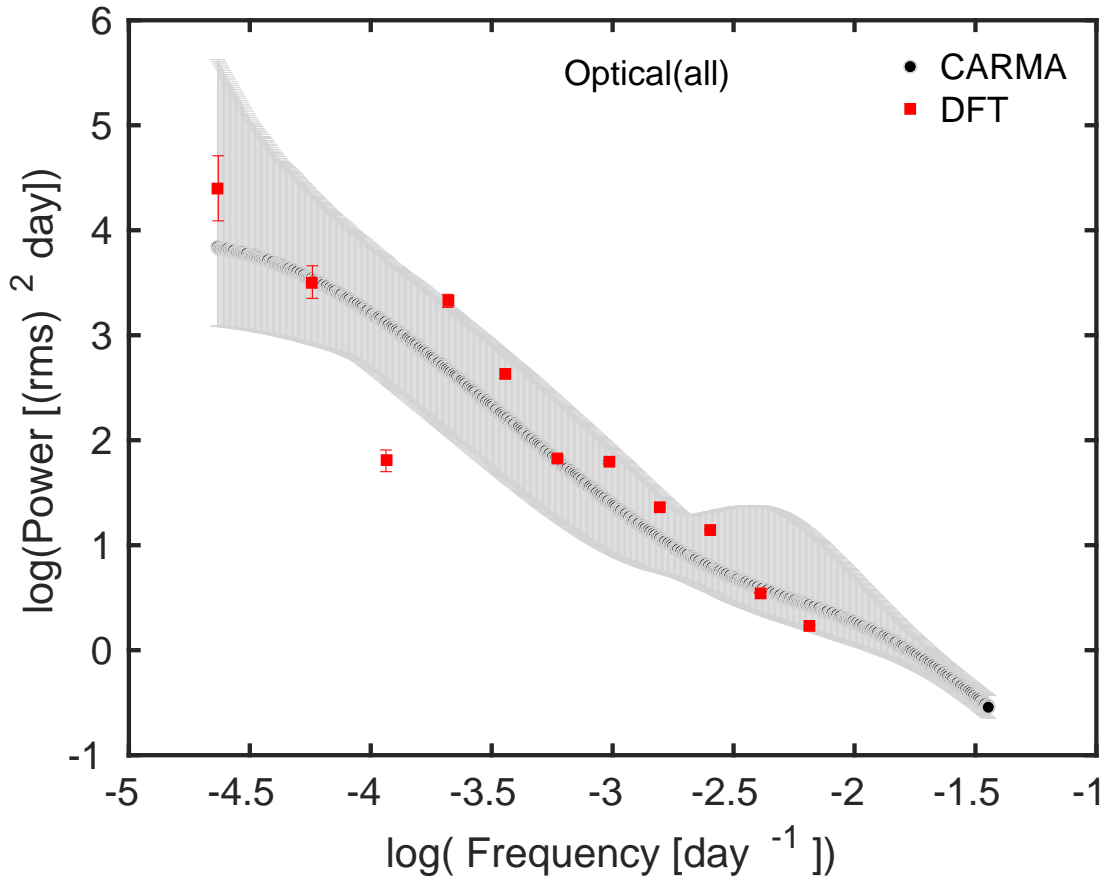


Figure 17. Power spectrum computed using DFT method (black) and CARMA modeling (red) with grey shaded regions corresponding to 3σ confidence intervals on the PSD estimates.

REFERENCES

- Abdalla, H., Abramowski, A., Aharonian, F., et al. 2017, *A&A*, 598, A39
- Abdo, A. A., Ackermann, M., Ajello, M., et al. 2009, *ApJS*, 183, 46
- . 2010, *ApJ*, 715, 429
- Acero, F., Ackermann, M., Ajello, M., et al. 2016, *ApJS*, 223, 26
- Ackermann, M., Ajello, M., Atwood, W. B., et al. 2015, *ApJ*, 810, 14
- Ackermann, M., Anantua, R., Asano, K., et al. 2016, *ApJ*, 824, L20
- Aharonian, F., Akhperjanian, A. G., Bazer-Bachi, A. R., et al. 2007, *ApJ*, 664, L71
- Aleksić, J., Antonelli, L. A., Antoranz, P., et al. 2011, *ApJ*, 730, L8
- Aller, H. D., Aller, M. F., & Hughes, P. A. 1985, *ApJ*, 298, 296
- Atwood, W. B., Abdo, A. A., Ackermann, M., et al. 2009, *ApJ*, 697, 1071
- Begelman, M. C., Blandford, R. D., & Rees, M. J. 1984, *Reviews of Modern Physics*, 56, 255
- Bevington, P. R., & Robinson, D. K. 2003, *Data reduction and error analysis for the physical sciences* (3rd ed., by Philip R. Bevington, and Keith D. Robinson. Boston, MA: McGraw-Hill, ISBN 0-07-247227-8, 2003)
- Bhatta, G., Zola, S., Stawarz, L., et al. 2016, *ApJ*, 832, 47
- Böttcher, M., Reimer, A., Sweeney, K., & Prakash, A. 2013, *ApJ*, 768, 54
- Burnham, K. P., & Anderson, D. R. 2004, in *New York : Springer, Vol. 54, Physics of Active Galaxies*, ed. G. V. Bicknell, M. A. Dopita, & P. J. Quinn, 91
- de Young, D. S. 2002, *The physics of extragalactic radio sources* (University of Chicago Press, 2002)
- Deeming, T. J. 1975, *Ap&SS*, 36, 137
- Edelson, R., Mushotzky, R., Vaughan, S., et al. 2013, *ApJ*, 766, 16
- Falomo, R., Pian, E., & Treves, A. 2014, *A&A Rev.*, 22, 73
- Finke, J. D., & Becker, P. A. 2015, *ApJ*, 809, 85
- Fiorucci, M., & Tosti, G. 1996, *A&AS*, 116, 403
- Foschini, L., Ghisellini, G., Tavecchio, F., Bonnoli, G., & Stamerra, A. 2011, *A&A*, 530, A77
- Gehrels, N., Chincarini, G., Giommi, P., et al. 2004, *ApJ*, 611, 1005
- Gelman, A., & Rubin, D. B. 1992, *Statistical Science*, 7, 457
- Ghisellini, G., Celotti, A., Fossati, G., Maraschi, L., & Comastri, A. 1998, *MNRAS*, 301, 451
- Glass, I. S. 1999, *Handbook of Infrared Astronomy*, ed. R. Ellis, J. Huchra, S. Kahn, G. Rieke, & P. B. Stetson (Cambridge University Press, Aug 13, 1999, page 63)
- Goyal, A., Stawarz, L., Ostrowski, M., et al. 2017, *ArXiv e-prints*, arXiv:1702.02504
- Howell, S. B., Soback, C., Haas, M., et al. 2014, *PASP*, 126, 398
- Hudec, R., Bašta, M., Pihajoki, P., & Valtonen, M. 2013, *A&A*, 559, A20
- Hurvich, C. M., & Tsai, C. L. 1989, *Biometrika*, 76, 297
- Isobe, N., Sato, R., Ueda, Y., et al. 2015, *ApJ*, 798, 27
- Kastendieck, M. A., Ashley, M. C. B., & Horns, D. 2011, *A&A*, 531, A123
- Kataoka, J., Takahashi, T., Wagner, S. J., et al. 2001, *ApJ*, 560, 659
- Kelly, B. C., Bechtold, J., & Siemiginowska, A. 2009, *ApJ*, 698, 895
- Kelly, B. C., Becker, A. C., Sobolewska, M., Siemiginowska, A., & Uttley, P. 2014, *ApJ*, 788, 33
- Kelly, B. C., Sobolewska, M., & Siemiginowska, A. 2011, *ApJ*, 730, 52
- Kushwaha, P., Chandra, S., Misra, R., et al. 2016, *ApJ*, 822, L13
- Liodakis, I., Pavlidou, V., Hovatta, T., et al. 2017, *ArXiv e-prints*, arXiv:1702.05493
- Lister, M. L., Aller, M. F., Aller, H. D., et al. 2016, *AJ*, 152, 12
- Massaro, E., Giommi, P., Perri, M., et al. 2003, *A&A*, 399, 33
- McHardy, I. M., Koering, E., Knigge, C., Uttley, P., & Fender, R. P. 2006, *Nature*, 444, 730
- Meier, D. L. 2012, *Black Hole Astrophysics: The Engine Paradigm* (Springer, Verlag Berlin Heidelberg, 2012)
- Nilsson, K., Takalo, L. O., Lehto, H. J., & Sillanpää, A. 2010, *A&A*, 516, A60
- O'Brien, S. 2017, *ArXiv e-prints*, arXiv:1708.02160
- O'Riordan, M., Pe'er, A., & McKinney, J. C. 2017, *ApJ*, 843, 81
- Qian, B., & Tao, J. 2003, *PASP*, 115, 490
- Rani, B., Lott, B., Krichbaum, T. P., Fuhrmann, L., & Zensus, J. A. 2013, *A&A*, 557, A71
- Revalski, M., Nowak, D., Wiita, P. J., Wehrle, A. E., & Unwin, S. C. 2014, *ApJ*, 785, 60
- Richards, J. L., Max-Moerbeck, W., Pavlidou, V., et al. 2011, *ApJS*, 194, 29
- Saito, S., Stawarz, L., Tanaka, Y. T., et al. 2013, *ApJ*, 766, L11
- Sandrinelli, A., Covino, S., Dotti, M., & Treves, A. 2016, *AJ*, 151, 54
- Seta, H., Isobe, N., Tashiro, M. S., et al. 2009, *PASJ*, 61, 1011
- Sillanpää, A., Takalo, L. O., Pursimo, T., et al. 1996, *A&A*, 305, L17
- Sobolewska, M. A., Siemiginowska, A., Kelly, B. C., & Nalewajko, K. 2014, *ApJ*, 786, 143
- Takalo, L. O. 1994, *Vistas in Astronomy*, 38, 77
- Takalo, L. O., Sillanpää, A., & Nilsson, K. 1994, *A&AS*, 107
- Timmer, J., & Koenig, M. 1995, *A&A*, 300, 707
- Ulrich, M.-H., Maraschi, L., & Urry, C. M. 1997, *ARA&A*, 35, 445
- Urry, C. M., & Padovani, P. 1995, *PASP*, 107, 803
- Valtonen, M., & Sillanpää, A. 2011, *Acta Polytechnica*, 51, 76
- Valtonen, M. J., Zola, S., Ciprini, S., et al. 2016, *ApJ*, 819, L37
- Vaughan, S., Uttley, P., Markowitz, A. G., et al. 2016, *MNRAS*, 461, 3145
- Villforth, C., Nilsson, K., Heidt, J., et al. 2010, *MNRAS*, 402, 2087
- Wagner, S. J., & Witzel, A. 1995, *ARA&A*, 33, 163
- Wills, B. J., Wills, D., & Breger, M. 2011, *ApJS*, 194, 19
- Wills, B. J., Wills, D., Breger, M., Antonucci, R. R. J., & Barvainis, R. 1992, *ApJ*, 398, 454
- Zola, S., Valtonen, M., Bhatta, G., et al. 2016, *Galaxies*, 4, 41